MASTERARBEIT / MASTER'S THESIS

Titel der Masterarbeit / Title of the Master 's Thesis

„ Investigating the affinity of metalloporphyrin (TMPyP-AU) for deoxyribonucleic and ribonucleic poly-(A) motif and at-tempt to localization of viral poly-(A) within HRV capsid "

verfasst von / submitted by

Mahbod Mousavian

angestrebter akademischer Grad / in partial fulfilment of the requirements for the degree of

Master of Science (MSc)

Wien, 2019/ Vienna 2019

Studienkennzahl lt. Studienblatt / degree programme code as it appears on the student record sheet:	A 066 830
Studienrichtung lt. Studienblatt / degree programme as it appears on the student record sheet:	Molekulare Mikrobiologie, Mikrobielle Ökologie und Immunbiologie
Betreut von / Supervisor:	ao. Univ.-Prof. Dipl.-Ing. Dr. Dieter Blaas / degree(s) first name family name

Contents

1 Abstract: 3

2. Introduction: 5

2.1 Picornaviridae family: 5

2.2 Rhinoviruses: 6

2.2 Virus structure: 7

2.3 Genome Organisation: 8

2.4 Infection cycle: 10

2.5 Porphyrins: 12

2.5.1 Porphyrin-metal complexes: 14

3 Material and Methods: 16

3.1 electrophoretic mobility shift assay method (EMSA): 16

3.1.1 Silver staining: 19

3.2 Spectrophotometry: 20

3.3 Electron microscopy: 21

3.3.1 Magnesium RNA Fragmentation: 22

3.4 NMR analysis: 24

4 Results: 25

4.1 Incubation of TMPyP-Au with the A_{50} oligonucleotide results in a shift in EMSA, whereas oligonucleotides T_{50} and R_{50} only show a marginal effect: 25

4.2 Incubation of oligonucleotide A_{50} with TMPyP-Au causes red shift at Q-band region: 29

4.3 Binding of either TMPyP-Cu or TMPyP-Au to A_{16} attenuates the H-signal in NMR spectroscopy: 33

4.4 Poly-(A) adopts secondary structures on incubation with TMPyP-Au: 37

5. Discussions and further ideas: 41

6. Supporting information: 43

Acknowledgment: 43

References: 44

1 Abstract:

In recent years, various methods have been developed to specifically localize selected proteins in tissue slices by electron microscopy (EM). Most of them make use of electron-dense gold, either directly attached to the protein of interest in the form of nanogold beads (1) or bound to metallothionein (2) fused to the target. Another technique is based on the oxidative polymerization of diaminobenzidine (DAB) to an osmophilic precipitate by oxygen radicals that are generated by irradiation of fluorescent dyes attached to the molecule of interest (3, 4). Even simultaneous localization of different proteins was recently realized via selective photopolymerization of DAB complexes containing cerium and praseodymium, respectively, and their individual imaging by employing energy filters (5). However, only a few methods have been described for the EM localization of biological components different from proteins, in particular of RNA sequence motifs (6). In an attempt to close this gap, we examined the possibility of specifically introducing electron-dense labels into poly-(A) tails of RNA molecules.

The aim of this research was it to set the stage for the localization of RNA sequence motifs, in particular the poly-(A) tail within the genomic viral RNA of rhinoviruses, either encapsidated in the protein shell of the native virus or during viral RNA egress. Porphyrin metal derivatives, especially porphyrin-copper, were shown to have high affinity for poly-(A) (7). On the other hand, we reasoned that gold might be easier to observe by using EM, because of its higher density. Water-soluble Porphyrin (TMPyP) and different porphyrin metal derivatives can interact with a wide range of double-stranded (ds) DNA, G-quadruplex, and other biological macromolecules (7). The dsDNA binding mode of porphyrin and metal porphyrins indicate a variety of binding modes such as partial intercalation, groove binding, and outside binding with self-stacking of the porphyrins. (7)

Therefore, in collaboration with the Technical University of Vienna (Cintulová, Daniela), we obtained the gold-porphyrin complex equivalent to the copper-porphyrin and investigated its specificity and affinity for poly-(A). The affinity of porphyrin copper for poly-(A) had been shown to be about 103 times higher when compared to porphyrin nickel and zinc (7).

By using spectrophotometry, electro migration shift assays (EMSA), and nucleic magnetic resonance (NMR) we demonstrated that gold-porphyrin indeed preferentially binds poly-(A) and that its affinity is may in a similar range as for the copper compound. Within the frame of this master thesis, it was not possible to investigate the next step, which was trying to localize the poly-(A) within the native virus or in the more permeable intermediate subviral A-particle using EM techniques.

2. Introduction:

2.1 Picornaviridae family:

The name '*Picornaviridae*' refers to the very small size of these viruses (pico = small) and the RNA genome material among this family. Some important human and animal pathogens like hepatitis A virus, poliovirus, foot-and-mouth disease virus, and rhinovirus belong to this family. Studying these viruses had an important impact on modern virology. Foot-and-mouth disease virus was the first cultured animal virus in 1898 and the first virus that could be propagated successfully in tissue culture was poliovirus (8), both members of the above family.

The 'Picornaviridae' family is divided into 47 genera as:

1. Aalivirus	2. Ailurivirus	3. Ampivirus	4. Anativirus	5. Aphthovirus
6. Aquamavirus	7. Avihepatovirus	8. Avisivirus	9. Bopivirus	10. Cardiovirus
11. Cosavirus	12. Crohivirus	13. Dicipivirus	★ 14. Enterovirus	15. Erbovirus
16. Gallivirus	17. Harkavirus	18. Hepatovirus	19. Hunnivirus	20. Kobuvirus
21. Kunsagivirus	22. Limnipivirus	23. Livupivirus	24. Malagasivirus	25. Megrivirus
26. Mischivirus	27. Mosavirus	28. Orivirus	29. Oscivirus	30. Parechovirus
31. Pasivirus	32. Passerivirus	33. Poecivirus	34. Potamipivirus	35. Rabovirus
36. Rafivirus	37. Rosavirus	38. Sakobuvirus	39. Salivirus	40. Sapelovirus
41. Senecavirus	42. Shanbavirus	43. Sicinivirus	44. Teschovirus	45. Torchivirus
46. Tottorivirus	47. Tremovirus			

Source: http://www.picornaviridae.com, The Pirbright Institute (Feb, 2019)

★ Refers to Enterovirus genera/rhinovirus/rhinovirus A, B and C

2.2 Rhinoviruses:

Human rhinoviruses (HRV) were discovered in the early 1950s and identified as the reason for the common cold. After about 60 years, the search for a cure for this virus illness is still ongoing. Every year and worldwide, HRV causes millions of upper respiratory tract infection in children as well as in the elderly, which leads to considerable economic loss due to the reduction of working hours and for medical care (9-11). However, HRV infection and co-infection with other viruses, such as HIV or bacteria, such as streptococcus, can cause serious illness among children and immunocompromised adults. Although HRV is most known for upper respiratory tract infections, recent studies implicate it in chronic pulmonary disease, asthma, and severe bronchiolitis developments (12).

Since the discovery of HRV, more than 160 serotypes have been identified and confirmed, which were classified into two categories depending on their phylogenetic similarity, genus HRV-A and HRV-B (13).

Furthermore, sensitive molecular differentiation studies including RT-PCR techniques revealed a third class of HRVs, namely HRV-C (14,15).

2.2 Virus structure:

The viral capsid plays different important rolls and it has number of functions during virus life cycle:

- It protects the viral genetic material extracellular RNases
- It attaches the virion to specific receptors exposed on the prospective host cell
- The three-dimensional capsid structure helps specific recognition and packaging of the viral RNA
- It delivers the viral genome through the plasma membrane of host cell

Rhinovirus is a member of picornavirus, none-enveloped with one single-stranded positive-sense RNA (~7200 bases) and an icosahedral capsid (16). The capsid consists of 60 copies of four structural proteins (VP1, VP2, VP3, and VP4). The three larger proteins of VP1, VP2 and VP3 surface on the external side of the capsid whereas VP4, the smallest capsid protein (~7 kDa) faces the inner side of the shell and is in intimate contact with the viral RNA. The virus particle has a diameter about 30 nm.

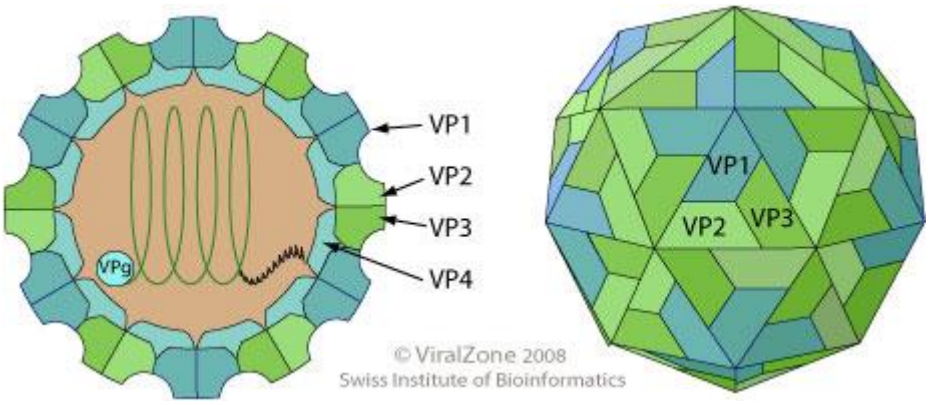

Figure 1: (left) Overall structure of picornaviral capsid with 60 protomers containing VP1, VP2 and VP3. (Right) One of the 60 protomers. Source: https://viralzone.expasy.org

2.3 Genome Organisation:

Picornaviruses have a single-stranded RNA genome of positive polarity that is on the order of 7,300 nt in length (16). A peptide, VPg (virion protein genome-linked), is covalently

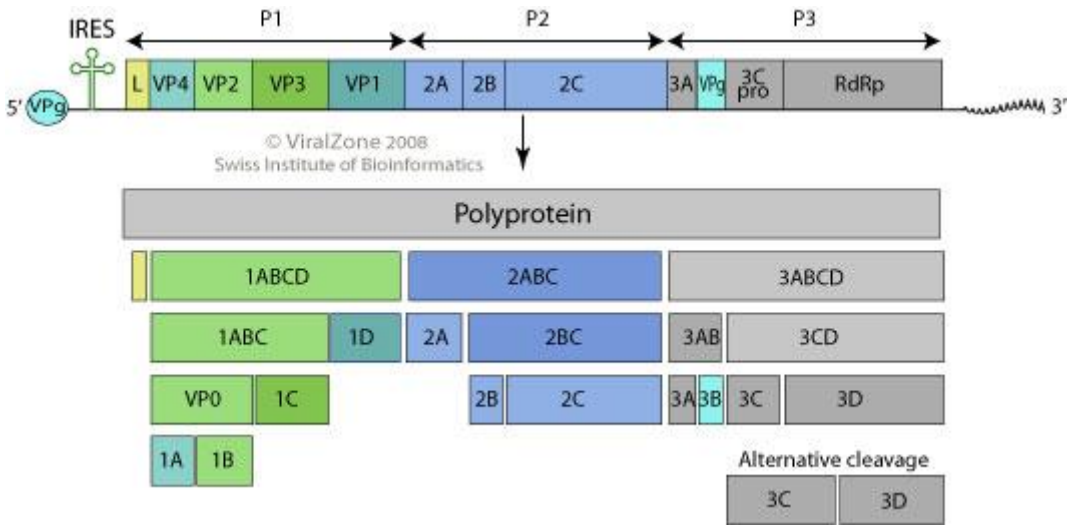

Figure 2: The overview of rhinoviruses genome with the proteolytic cleavage sites and the three resulting proteins Source: https://viralzone.expasy.org

linked to the 5'-end of the viral genome and a poly-(A) tail is present at the 3'-end. Genome replication occurs in a process, which uses the plus-strand as a template for synthesis of minus-strands, which, in turn, are used as a template to produce an excess of plus-strands. The genome can be divided into three main regions: the 5' untranslated region (5' UTR), a single open reading frame, 3' UTR, and the poly-(A). The 5' end of the RNA genome lacks a m^7G cap-structure, as found in cellular mRNAs but it is covalently bonded to VPg. During infection, the viral capsids expand by about 4%, with concomitant loss of VP4 and exposure of the N-terminal sequences of VP1.

In rhinoviruses, the conformational changes of the capsid are triggered by a decrease of the pH in endosomes. At first, the inner viral protein VP4 becomes lost and the native virus is converted into an intermediate subviral particle called ‘A-particle’ (17). It sediments at 135S as opposed to native virus, sediment at 150S. Due to the expansion of the capsid, the nucleic acid is subsequently released, presumably through one of the small pores that open at the icosahedral twofold-axes (18) and leaving behind an empty capsid called ‘B-particle’ (sediment at 80S) behind, which degraded inside the late lysosome.

Nonetheless, little is known about the change of organization of the RNA on conversion of the native virion into the A-particle. Because the RNA was shown to exit with the 3’ poly-(A) tail first, we asked the question of whether it was localized close to the point of it exit already in the native virion and/or the A-particle as suggested by encapsidation of the RNA starting with the 5’-end and finishing with the 3’-end (18). This should lead to a ‘last in first out’ situation. Furthermore, we asked whether the RNA is organized/folded similarly in all viral particles, with conserved sites of interaction with the protein shell, or is it a random coil. The work described below was meant at finding ways of localizing the 3’-end and/or the poly-(A) tail within the native virion or at least within the more permeable A-particle.

Although there are various methods for the localization of selected proteins in biological material by using, electron microscopy (EM) there is essentially none for the localization of specific RNA sequence motives, e.g. the poly-(A) tail e.g. of the above viruses via electron-dense tracers, like gold. We thus reasoned that specific attachment of many TMPyP-Au molecules along a poly-(A) stretch might increase its thickness as well as its electron density even more as in case of porphyrin copper derivatives.

Our aim in this research was it to find an electron dense compound which may facilitate localization of the 3' poly-(A) tail of the virus outside or within the subviral A-particle to improve our understanding about viral RNA folding during encapsidation and egress and its orientation inside the native virus.

2.4 Infection cycle:

The main site of RV infections is the nasal mucosa. The nasal cavity is lined by a pseudostratified epithelium composed of columnar, ciliated epithelial cells, mucous secreting goblet cells, and basal cells. HRVs are non-enveloped with an icosahedral protein capsid, which has 60 copies of the four viral proteins VP1–VP4 (16). Based on phylogeny, more than 160 HRV types were classified into species A, B, and C (13). Twelve HRV-A (the minor group) bind members of the low-density lipoprotein receptor (LDLR) family whereas the rest of A and B types (the major group) bind intercellular adhesion molecule-called (ICAM-1)(19); for HRV-C, the recently identified and CDHR3 serves as a receptor (20). The mechanisms of entry and uncoating of HRV-C is still not entirely understood; therefore, I shall limit the discussion to HRV-A and B.

Infection is triggered upon the cognate receptor becoming accessible to the virus i.e., at the apical surface of ciliated epithelial cells. HRVs of species A and B investigated so far enter cells by receptor-mediated endocytosis (21). In the endosomal lumen, they convert into subviral A (altered) particles devoid of the innermost capsid protein VP4 but still containing the RNA genome. After the release of the RNA (uncoating) into the cytoplasm, empty capsids remain (Fig. 3). Minor group HRVs exclusively depend on the low endosomal pH for this conformational modification and uncoating occurs even at 20 °C (21). Once the RNA has arrived in the cytoplasm, it is translated into a polyprotein. After autocatalytic cleavage into the structural (capsid) and non-structural proteins, the RNA is replicated by the viral polymerase. Finally, infectious progeny is assembled and released into the nasal cavity (22). In contrast to HRV infection in tissue culture cells, airway epithelial cells of patients are not lysed for virus release; as shown for other enteroviruses, it is thus possible that cell-to-cell spread might occur via virus-carrying micro-vesicles (23).

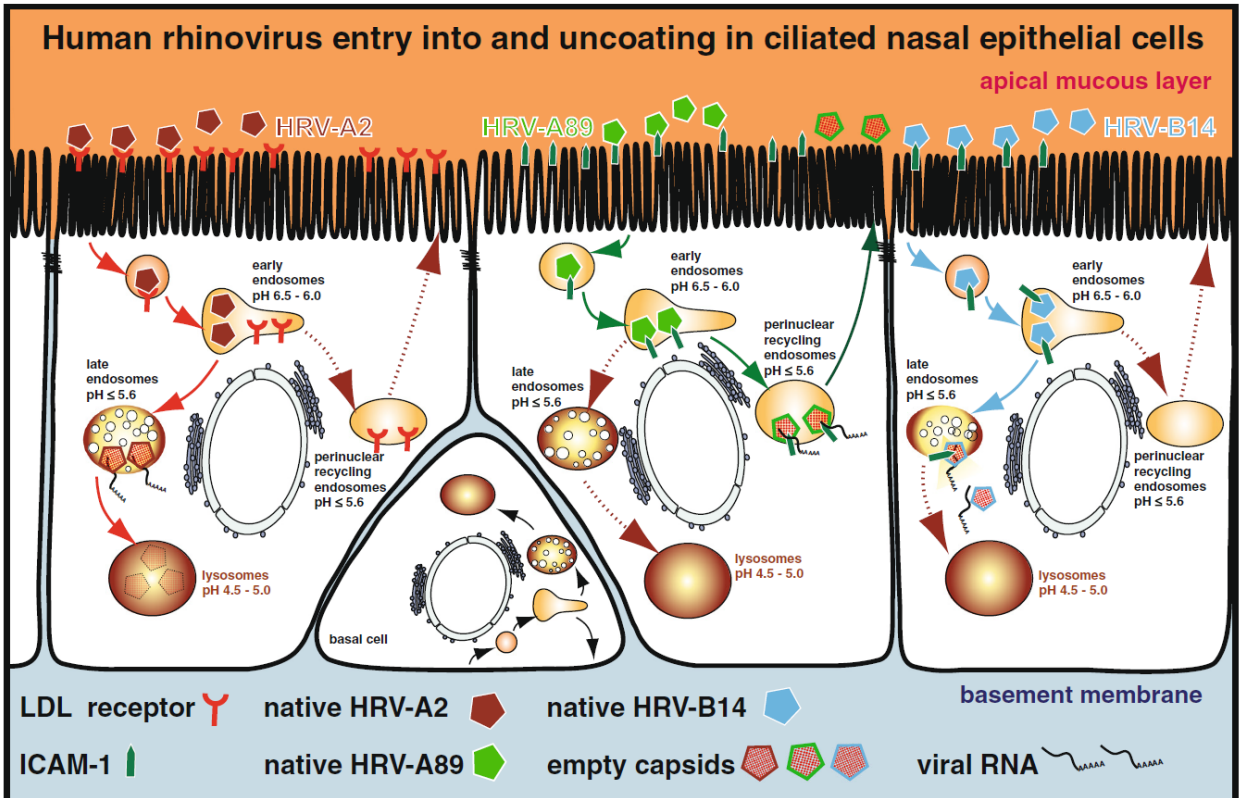

Figure 3: HRV entry and uncoating in ciliated nasal epithelial cells. Left, HRV-A2; middle, HRV-A89; and right, HRV-B14. For clarity, minor group and major group receptors (LDLR and ICAM-1, respectively) are depicted separately although they are co-expressed at the ciliated (apical) side of nasal epithelial cells as well as on the entire plasma membrane of basal cells. After binding to the respective receptor at the ciliated surface, the viruses are internalized and delivered into early endosomes. For HRV-A2, the mildly acidic pH in these compartments leads to dissociation of the virus from its receptor. While LDLR is returned to the apical plasma membrane via perinuclear recycling endosomes, the virus is directed to late endosomes. The low pH ≤ 5.6 in late endosomes converts native viruses into subviral A particles. Subsequently, the viral RNA is released and the remaining empty capsids (subviral B particles) are shuttled to and degraded in lysosomes. In contrast, HRV-A89 together with ICAM-1 is sorted into the recycling pathway. Perinuclear recycling endosomes are similarly acidic as late endosomes resulting in conversion of native HRV-A89 into A and then into B particles. After the transfer of the viral RNA into the cytoplasm, empty capsids are most likely returned to the apical mucous layer. After binding to the same receptor, HRV-B14 is routed from early endosomes into the pathway to lysosomes. However, after undergoing the ICAM-1-dependent conformational modification, the virus ruptures the endosomal membrane leading to RNA uncoating and its penetration into the cytoplasm. Thus, the viral capsid as well as the viral RNA escapes lysosomal degradation. So far, the fate of ICAM-1 is unknown. (24)

2.5 Porphyrins:

Porphyrins (which comes from the Greek for “purple”) are a ubiquitous class of naturally occurring molecules involved in a wide variety of important biological processes ranging from oxygen transport to photosynthesis, from catalysis to pigmentation changes (25). The common feature of all these molecules is the basic structure of the porphine (Fig 4) macrocycle, which consists of a 16-atom ring containing a central metal ion. The macrocycle is an aromatic system containing 22 π-electrons, but only 18 of them are delocalized according to the Hückel’s rule of aromaticity (4n+2 delocalized π-electrons, where n=4) (26).The size of the macrocycle is perfect to bind almost all kinds of metal ions and indeed a number of metals (e.g. Fe, Zn, Cu, Ni, and Co) were inserted in the center of the macrocycle forming metalloporphyrins. Porphyrin-based fundamental biological representatives include hemes, chlorophylls, vitamin B12, and several others. Heme proteins (which contain iron porphyrins) serve many roles, like O2 storage and transport (myoglobin and hemoglobin), electron transport (cytochromes b and c), and O2 activation and utilization (cytochrome P450 and cytochrome oxidase). Chlorophylls (which have a central magnesium ion) and pheophytins (which are metal free) are found in the photosynthetic apparatus of plants and bacteria, while vitamin B-12 (which has cobalt) is present in bacteria and animals (26).

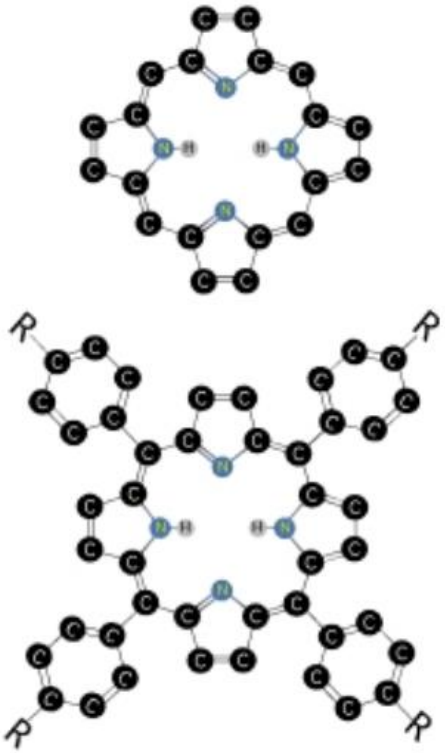

Figure 4: structure of the porphine macrocycle (top) and of tetraphenyl-porphyrin (bottom). The hydrogen atoms saturating the carbon bonds are not shown. The R-groups may indicate: alkyl-, alkoxy-, amino-, carboxyl-, carbomethoxyl-,halogeno- and nitro-groups. Source: PORPHYRINS: FASCINATING MOLECULES WITH BIOLOGICAL SIGNIFICANCE

Given the capabilities of porphyrins to bind and release gases and to act as active center in catalytic reactions in biological systems, porphyrin-based films on metal or semiconductor surfaces are extremely appealing as chemical and gas sensors (27) as well as nanoporous catalytic materials (28) in novel synthetic bio-mimetic devices. Moreover, the role of porphyrins in photosynthetic mechanisms indicates a good attitude of these molecules to mediate visible photon – electron energy transfer processes.

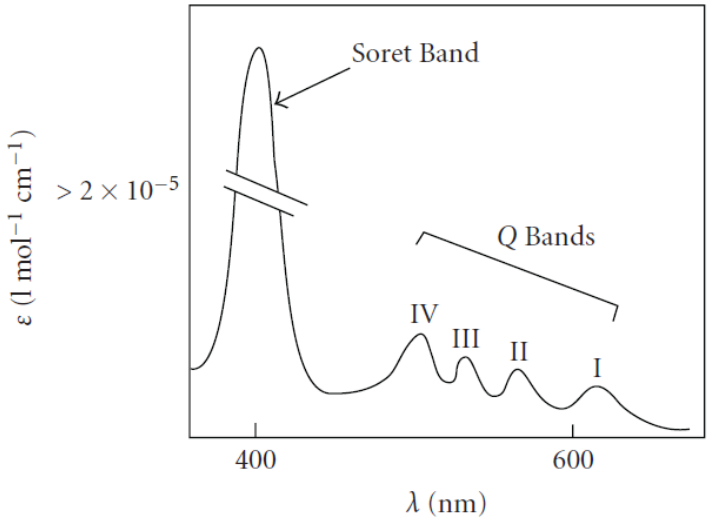

Figure 5: Typical Porphyrin absorption (26)

As shown in Figure 3, the UV-visible absorption spectrum of the highly conjugated porphyrin macrocycle exhibits intense absorbance (extinction coefficient > 200.000) at about 400 nm (the “Soret” band), followed by several weaker bands (Q bands) at higher wavelengths (from 450 to 700 nm). While variations of the peripheral substituents on the porphyrin ring often cause minor changes to the intensity and wavelength of the absorption features, protonation of two of the inner nitrogen atoms or the insertion/change of metal atoms into the macrocycle usually strongly change the visible absorption spectrum. For this reason, in recent years, (metallo) porphyrins and porphyrin-metal interfaces have become of major interest for applications in opto-electronics, data storage and solar cells (29) and a still increasing number of covalently linked donor-acceptor supramolecular porphyrin-based assemblies have been studied for these purposes (30).

2.5.1 Porphyrin-metal complexes:

Small molecules that bind selectively and with high affinity to single-stranded nucleic acids are considered rare (7). However, such molecules have a high potential to be used as tools to solve open questions in various biological fields. Therefore, investigating their interaction with DNA and RNA in detail is essential for any further studies of RNA motives. One example is the interaction of metal complexes derived from porphyrins with guanine quadruplexes, which have been studied by various research groups since a few years with respect to anticancer treatment (7).

Porphyrinoids are ideal compounds to be inserted into DNA due to their peculiar characteristics: 1: high molar absorptivity coefficient of the main absorption band (Soret band) owing to the large aromatic structure; 2: the possibility to tune the electronic properties of the molecules by implementing small variations in the macrocycle ring or introducing metal ions in the core; 3: absorption spectrum in the 360–750 nm range, which lies outside the spectroscopic absorption range of nucleic acids; and 4: the ability to act as photosensitizers in the presence of oxygen in photo therapy.

metal	RNA	K_b (M^{-1})	H (%)	$\Delta\lambda$ (nm)
Zn	total RNA	$(1.99 \pm 0.16) \times 10^6$	31.3	12
	tRNA	$(1.81 \pm 0.15) \times 10^6$	33.4	12
	poly(A)	$(2.00 \pm 0.12) \times 10^8$	64.0	19
Cu	total RNA	$(2.26 \pm 0.15) \times 10^6$	45.6	9
	tRNA	$(2.52 \pm 0.18) \times 10^6$	46.5	9
	poly(A)	$(8.17 \pm 0.63) \times 10^8$	67.3	17
Ni	total RNA	$(1.67 \pm 0.14) \times 10^6$	34.5	9
	tRNA	$(1.90 \pm 0.11) \times 10^6$	31.1	10
	poly(A)	$(3.57 \pm 0.21) \times 10^8$	53.9	20

Figure 6: Hyperchromic (H) and Red shift (Δλ) of Soret Band in Absorption Spectra of M-TMPyP (5 mM Tris-HCl, 50 mm NaCl, pH 7.0) upon addition of RNA and Calculated Binding Constants (Kb) (7)

The Porphyrin-copper complexes have been shown to bind with up to 100-fold higher affinity to poly-(A) compared to random RNA sequences (7) making them particularly interesting as probes to identify poly-(A) stretches in nucleic acids. This was the reason for their characterization within this work.

The selectivity of the Cu-complex was substantially higher than that of Ni- and Zn-complexes (7). It can be assumed that attachment of multiple such molecules results in substantially increased contrast, which might even be higher when copper is replaced with gold. Therefore, we first investigated the binding of a porphyrin gold to single-stranded DNA. The presence of gold as the center atom in the porphyrin complex allowed us to identify the binding affinity using nuclear magnetic resonance spectroscopy (NMR) and we hoped that it would also allow localizing poly-(A) within the viral RNA by electron microscopy (EM) techniques.

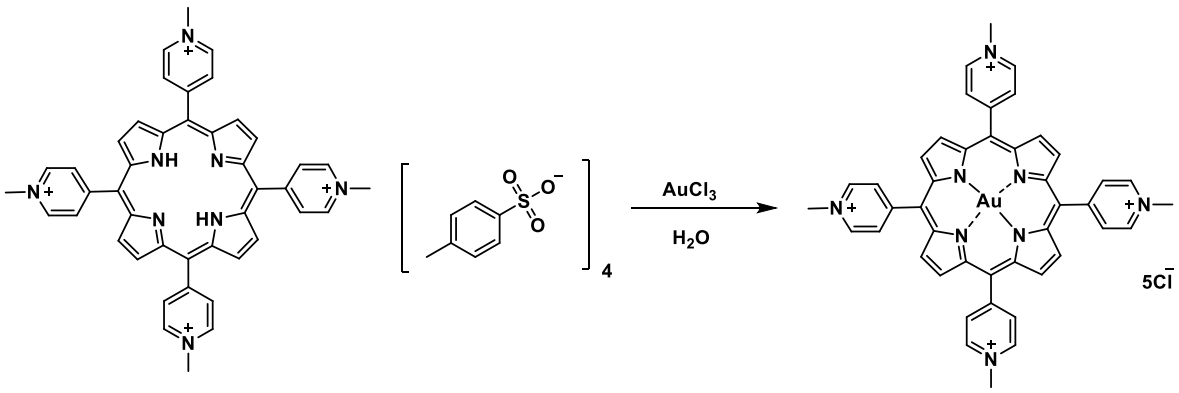

Figure 7: TMPyP-Au structure

Based on the above, we hypothesized that using porphyrin gold we might be able to detect the poly-(A) tail of the viral RNA within the capsid and thus allow determining the orientation of the RNA inside the viral shell and RNA egress during uncoating.

3 Material and Methods:

All ssDNA oligonucleotides were ordered and purchased from Microsynth, Austria and dissolved in Milli-Q or DEPC treated water to a final concentration of 100 µM. Other concentrations were made by diluting this stock.

The chemicals mentioned below, and all other chemicals used were of analytical grade and were obtained from various commercial sources.

3.1 electrophoretic mobility shift assay method (EMSA):

To test the overall affinity of Au-porphyrin complex for oligonucleotides, we started our pilot experiments using ssDNA oligonucleotides. Working with DNA is much easier because of its higher stability. If degradation can be excluded, the results are more reliable, although the real goal was testing the affinity of TMPyP-Au for different RNA oligonucleotides and finally for viral RNA. Control experiments showed that the results with ssDNA and ssRNA of the same sequence were comparable.

To do this, oligonucleotides with different sequences such as A_{50}, T_{50}, and a random sequence R_{50} used during electrophoretic mobility shift assay (EMSA) and spectrophotometric experiments. EMSA was performed using different concentrations of TMPyP-Au with each oligonucleotide at constant concentration. The optimal concentration of TMPyP-Au for shifting oligonucleotide bands in a gel was found out by incubation of different concentrations of TMPyP-Au and oligonucleotides. It was observed that TMPyP-Au concentrations higher than 200 µM precipitated fast on addition of oligonucleotides. Such aggregates of nucleic acid and TMPyP-Au is not able to migrate into polyacrylamide gel during electrophoresis. Therefore, four different concentrations (10, 50, 100 and 200 µM TMPyP-Au) were tested with 100 µM of different oligonucleotides for (EMSA) assay.

The principle of the electrophoretic mobility shift assay is straightforward and widely used approach. This assay is relatively quick and easy and utilizes equipment available in most laboratories; however, there are many variables that can only be determined empirically; therefore, optimization is necessary and can be highly dependent upon the system (31).

Different concentrations of TMPyP-Au were incubated at 25° and applied onto a 20% native polyacrylamide gel. The polyacrylamide gels, acrylamide:bisacrylamide (29:1), was made using the standard procedure with 10, 15 and 20 percent acrylamide employing Milli-Q water.

Staining of the oligonucleotide T_{50} is not possible by using silver because of the competitive inhibition, which could be affected by the amounts of the argyrophil nucleobase and base T, the cis-distance between the argyrophile nucleobase and base T, and the gel concentration. The sensitivity of DNA oligonucleotides A_{50}, C_{50} and T_{50} to silver staining in the range (dA) > (dC) > (dT) from high to low (32).

Oligonucleotide dA_{50}:

3´.AAAAAAAAAAAAAAAAAAAAAAAAAAAAAAAAAAAAAAAAAAAAAAAAAA 5´

Oligonucleotide dT_{50}:

3´ TTTTTTTTTTTTTTTTTTTTTTTTTTTTTTTTTTTTTTTTTTTTTTTTTT 5´

Oligonucleotide dR_{50}:

3´ ATCGATCGATCGATCGATCGATCGATCGATCGATCGATCGATCGATCGAT 5´

The gels are prepared as follows: horizontal 2% agarose gel with 60 mm x 60 mm x 1.5 mm (length x width x thickness) were prepared with a Tris-borate (TBE) buffer (10 mM EDTA, 450 mM Tris, 450 mM Boric Acid, pH=8.3). DNA markers were diluted with the included sample buffer.

For the PAGE assay, 20% polyacrylamide gels (80 mm x 100 mm x 0.75 mm) were prepared using a Tris-borat (TBE) buffer (10 mM EDTA, 450 mM Tris, 450 mM Boric Acid, pH=8.3) and 29:1 acrylamide:bisacrylamide. Four ml of 29:1 acrylamide:bisacrylamide was mixed with 1.2 ml of 5X TBE buffer and the final volume was adjusted to 6 ml using 0.8 ml of milli-Q water. 100 µl APS and then 5 µl of TEMED were wadded, mixed with other reagents, and instantly poured into the gel cassette. Samples were mixed at room temperature (≈25˚C) and incubated at 37˚ for 15 minutes prior to loading the samples. Gels were run at 100 V for 2 hours and bands were revealed by using a silver staining method.

3.1.1 Silver staining:

Silver staining is known to be a highly sensitive but rather unspecific staining method for proteins and nucleic acids. Silver staining is more sensitive than ethidium bromide for ds-DNA but also detects ss-DNA and RNA with similar sensitivity (33). The method relies on the reduction of silver by nucleic acids but the mechanism by which nucleic acids reduce silver ions is not well defined. The only drawback of this method is lack of staining of thymidine; staining intensity is thus inversely related to the number of thymidine nucleotides. Inhibition of silver staining of thymine is via competition, which could be affected by the amounts of the argyrophil nucleobase and base T, the cis-distance between the argyrophil nucleobase and base T, and the gel concentration (32). The procedure was applied as follows; after the run of the gel was completed, it was washed twice with deionized water before incubating it in the fixing solution (12% glacial acetic acid, 50% EtOH (96%), 0.005% formaldehyde (37%), 37.95% dH_2O) at 4°C overnight or at least 4 hours. After discarding the fixation solution, the gel was washed 3 times with 20% EtOH, each time for 2 minutes following twice with dH_2O for one minute. Then, the silver staining solution was discarded, and the gel was washed twice with dH_2O for 20 seconds and the developing solution (6% Na_2CO_3, 0.0004% $Na_2S_2O_3$, 0.0005% formaldehyde (37%)) was added. Now, the gel was developed for 1-5 minutes; when the bands were dark enough to be easily distinguished, the reaction was terminated with a stop solution (12% acetic acid). The gels were documented by using a ChemiDoc device (34).

3.2 Spectrophotometry:

Spectrophotometry was performed by mixing increasing concentrations of oligonucleotides with TMPyP-Au at a constant concentration. This leads to spectral changes in the Soret and Q-bands. However, because of the high absorbance at the Soret band (340 nm) we rather concentrated on spectral changes of the Q-bands (between 500 and 550 nm).

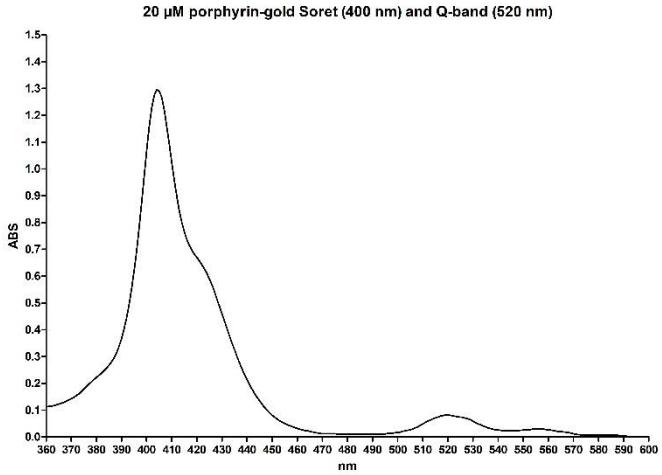

Figure 8: TMPyP-Au absorption

UV-Vis spectroscopic titrations were carried out using a Hitachi U-3501 spectrophotometer at 25 °C using a quartz cuvette (105-251-15-40, Hellma Analytics). A solution of 100 µM TMPyP-Au was prepared and 200 µl of it was transferred into the cuvette; the titration was performed in thirty steps, 1 µl each of the respective oligonucleotide, A50 and T50. Oligonucleotide concentration was 0-3 µM in 30 steps. The dilution of TMPyP-Au resulting from the addition of the oligonucleotide solution was considered via normalization. Absorption spectra were collected from 500 nm to 550 nm. The quartz cuvettes were always thoroughly cleaned with isopropanol and milli-Q water to remove traces of TMPyP-Au or DNA. The difference in the absorption maxima and the wavelength-shift of the Q-band were recorded using the computer attached to the spectrophotometer; the final plot was realized by using GraphPad prism8 software. As a negative control, the experiment was repeated by using plain Milli-Q water instead of TMPyP-Au.

3.3 Electron microscopy:

We also attempted to detect binding of TMPyP-Au to poly-(A) as an increase in thickness by rotary shadowing electron microscopy; fragmented poly-(A) was incubated with/without 100 µM TMPyP-Au, applied to mica by spraying, shadowed with 0.7 nm platinum, transferred to carbon-coated grids and viewed at 36,000 and 71,000 x. Samples were diluted to a final concentration of 50-100 µg/ml poly-(A) in spraying buffer (100 mM ammonium acetate, 30% (v/v) glycerol, pH adjusted to 7.6), sprayed onto freshly cleaved mica chips (Christine Gröpl, Austria) and immediately transferred into a BAL-TEC MED020 high vacuum evaporator (BAL-TEC, Liechtenstein) equipped with electron guns. While rotating, samples were coated with 0.7 nm platinum (BALTIC, Germany), at an angle of 4°, followed by 6-8 nm carbon (Balzers, Liechtenstein) at 90°. The obtained replicas were floated off under water from the mica chips, picked up on 400 mesh Cu/Pd grids (Agar Scientific, UK), and inspected in a FEI Morgagni 268D TEM (FEI, Netherlands) operated at 80kV. Images were acquired using an 11-megapixel Morada CCD camera (Olympus-SIS, Germany). For control purposes, the same experiment was carried out with *in-vitro* synthesized ss RNA.

3.3.1 Magnesium RNA Fragmentation:

The poly-(A) RNA purchased from Merck (10108626001, Roche) has a chain length of 2,100 to 10,000 nucleotides. Molecules of these lengths tend to coil during the spraying procedure; therefore, the RNA was fragmented to about 200 nucleotides by using the 'Magnesium RNA fragmentation module' (E6150S) from New England Bio labs.

Starting Material: poly-(A) RNA (50–250 ng)

1. 2 µl of RNA fragmentation buffer (10X) was mixed with 1-18 µl of the poly-(A) RNA and the total volume was adjusted to 20 µl using nuclease free water in a clean, nuclease free PCR tube.
2. The above sample was incubated in a preheated thermal cycler for 1–5 minutes at 94°C and into ice.
3. Two µl of 10X RNA Fragmentation Stop Solution was added.
4. The fragmented RNA was then stored at -80°C until use.

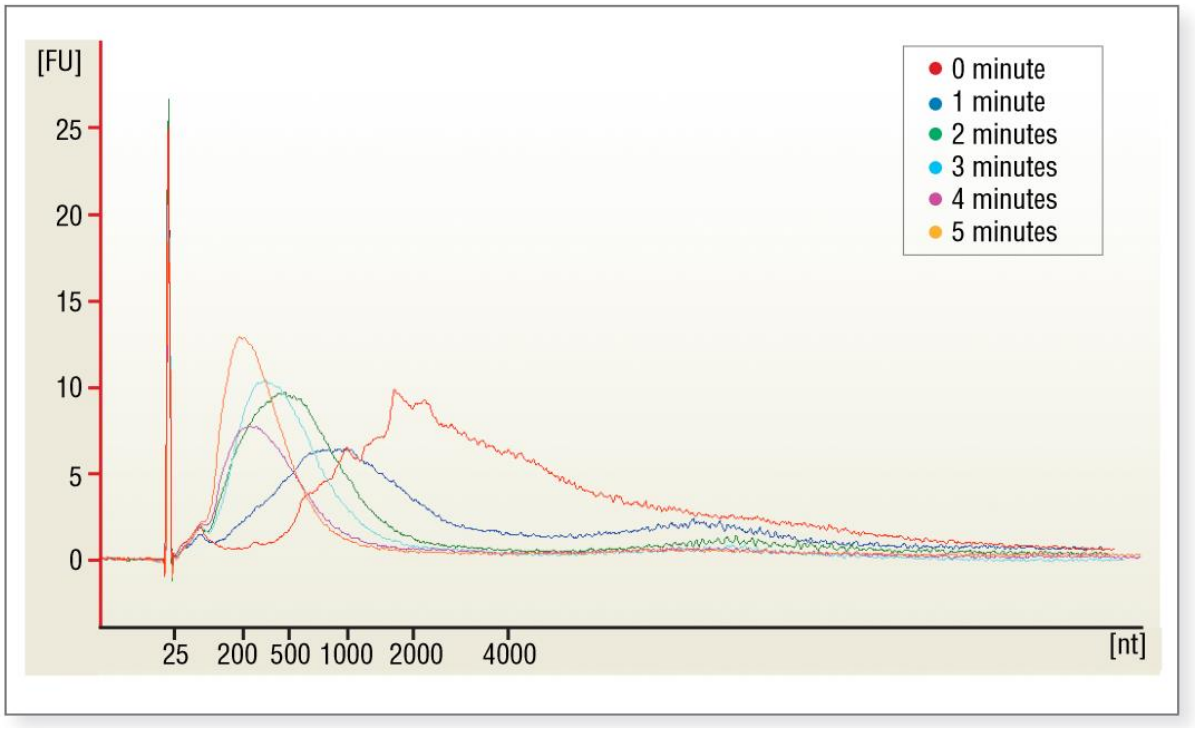

Figure 9: Poly (A)+ mRNA (40 ng) purified from the Universal Human Reference Total RNA (Stratagene) was fragmented in 1X NEBNext Magnesium RNA Fragmentation Buffer for 1–5 minutes at 94°C. Fragmentation Reaction was stopped in 1X NEBNext Fragmentation Stop Solution. Samples were diluted 1:10 in Nuclease-Free Water and analysed in the Bioanalyzer 2100. Source: Copied from the website of 'neb.com'

Based on the above, an incubation time of 5 minutes was chosen in our experiments.

3.4 NMR analysis:

NMR analysis was carried out by preparing solutions of TMPyP-Au and TMPyP-Cu at 100 μM, each. Spectra were recorded by the Georg Kontaxis, Department of Structural and Computational Biology at VBCF. Titration of the oligonucleotides dA_{16} and dR_{16} (see below), was performed by using a stock solution of 100 μM. The oligonucleotides were titrated against a constant concentration of TMPyP-Au using the LOGSY method because of the diamagnetic property of gold. WaterLOGSY is a popular ligand-observation NMR technique. It is mainly used for the screening of protein-ligand interactions. Yet, when applied to measure dissociation constants (K_D) through ligand titration, the results were found to be strongly dependent on the nature of the sample (35). On the other hand, because of the paramagnetic properties of copper, TMPyP-Cu was titrated against a constant concentration of each oligonucleotide and changes of the spectrum of the oligonucleotide were recorded.

Oligonucleotide dA_{16}: 3′ AAAAAAAAAAAAAAAA 5′

Oligonucleotide dR_{16}: 3′ ATCGATCGATCGATCG 5′

4 Results:

4.1 Incubation of TMPyP-Au with the A_{50} oligonucleotide results in a shift in EMSA, whereas oligonucleotides T_{50} and R_{50} only show a marginal effect:

The ssDNA oligonucleotides A_{50}, R_{50}, and T_{50} were incubated with TMPyP-Au at different concentrations. At high concentrations of TMPyP-Au precipitation was observed upon addition of DNA/RNA preventing entry into the gel. The optimal concentration, avoiding precipitation but showing a strong migrational shift, was determined by incubating the different oligonucleotides at different TMPyP-Au ratios; four TMPyP-Au concentrations, 10, 50, 100, and 200 µM were assessed, keeping the oligonucleotide concentration constant at 10 µM. This results in ratios of 1:1, 5:1, 10:1, and 20:1 for TMPyP-Au: oligonucleotide, respectively.

For EMSA, only A_{50} and R_{50} were used because of the above-explained lack of silver staining of T. Furthermore, G_{50} was also not included in the experiment because, according to the manufacturer, it is difficult to produce; guanines are known to bind to each other, which is reflected in secondary structures known as G-quadruplexes. This is manifested when running a native polyacrylamide gel; ssDNA G oligonucleotides produce smears (not shown).

After incubation of A_{50} with different concentrations of TMPyP-Au, the samples were run in native polyacrylamide gels following silver staining. At a concentration of 10 µM TMPyP-Au, no significant band shift was apparent, but a shift was evident from 50 µM onward. At 200 µM, the highest concentration assessed, most of the lower band had disappeared and had been replaced by a band migrating on top of it (Fig. 10); because of precipitation, no higher concentrations were studied. In contrast, no shift was observed for the R_{50} oligonucleotide (see above) at the lower concentrations, and only a small shift was apparent at the highest concentration (200 µM; see Fig. 11); the marginal effect of TMPyP-Au on R_{50} might be related to the presence of 25% of adenines in this sequence.

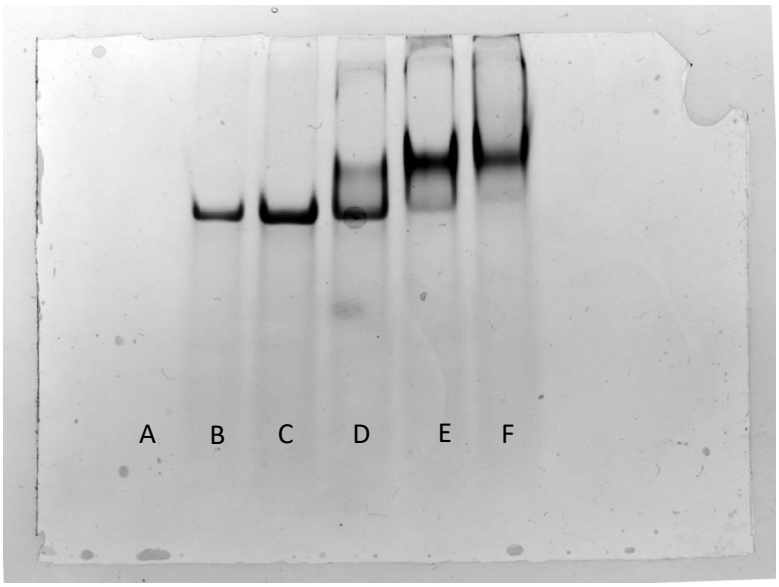

Figure 10: Oligo A_{50} 10µM with TMPyP-Au, 20% Polyacrylamide native gel, silver stained.

From left **(A)** TMPyP-Au, **(B)** ssDNA A_{50}, **(C)** ssDNA A_{50} + 10µM TMPyP-Au, **(D)** ssDNA A_{50} + 50µM TMPyP-Au, **(E) ssDNA** A_{50} + 100µM and **(F)** ssDNA A_{50} + 200µM TMPyP-Au

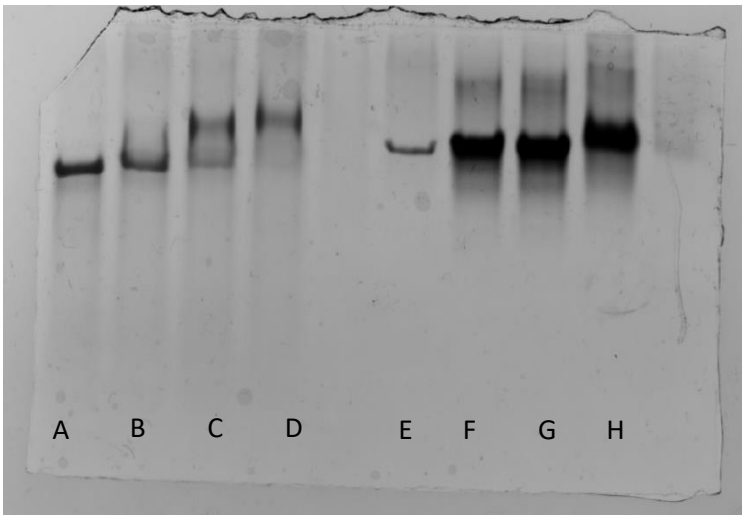

Figure 11: Oligonucleotide A_{50} and R_{50} 10µM with TMPyP-Au, 20% Polyacrylamide native gel, silver stained.

From left **(A)** ssDNA A_{50} ,**(B)** ssDNA A_{50} + 50µM TMPyP-Au, **(C)** ssDNA A_{50} + 100µM TMPyP-Au, **(D)** ssDNA A_{50} + 200µM TMPyP-Au following **(E)** ssDNA R_{50} ,**(F)** ssDNA R_{50} + 50µM TMPyP-Au, **(G)** ssDNA R_{50} + 100µM TMPyP-Au, **(H)** ssDNA R_{50} + 200µM TMPyP-Au.

As controls, and to check whether the observed specific shift also occurred with RNA, the EMSA experiment was repeated, this time by using fragmented poly-(A) RNA and total E. coli RNA. Both had been subjected to fragmentation to about 200 nt by using the above magnesium fragmentation module. On incubation with 200 µM TMPyP-Au, the samples were analyzed on a 2% agarose gel that had been pre-stained with Midori green advance (MG04, Bulldog Bio. Inc). As seen in Fig. 12, the poly-(A) band shifted from about 200 nt to about 350 nt on incubation with 200 µM TMPyP-Au. No such shift was apparent for the fragmented total E. coli RNA.

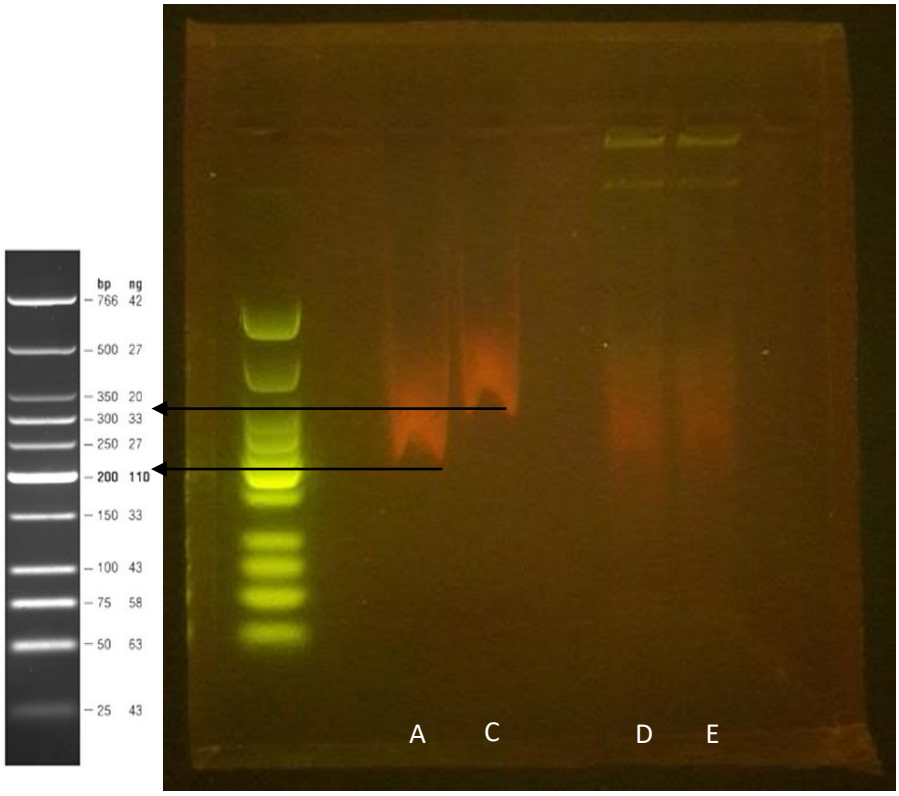

Figure 12: Poly-(A) RNA and total RNA of about 200 nt were incubated with 200µM TMPyP-Au and run on a 2% agarose gel. Staining was with midori green advance. The poly-(A) shifted from a position roughly corresponding to 200 nt to 350 nt on incubation with 200 µM TMPyP-Au. From left: **(A)** Ladder, **(B)** poly-(A), **(C)** poly-(A) + 200 µM TMPyP-Au, **(D)** total E. coli RNA and **(E)** total E. coli RNA + 200 µM TMPyP-Au. Note that the RNAs had been fragmented to a mean size of 200 nt.

Our attempts at silver staining the oligonucleotide T_{50} were not successful; therefore, we used methylene blue, another nucleic acid stain, to compare the effect of TMPyP-Au on gel migration of the A_{50} and T_{50} oligonucleotides. According to the manufacturer (Microsynth GmbH), ssDNA oligonucleotides of the same lengths but with different sequences exhibit quite different gel-migration speeds, with G < T < A < C. This explains why in Fig. 13, A_{50} and T_{50} show a substantially different migration, even in the absence of TMPyP-Au (compare lanes A and E). However, addition of TMPyP-Au has no influence on the migration of T_{50} (E to H), whereas, at 200 µM, TMPyP-Au substantially decreases the migration of A_{50}.

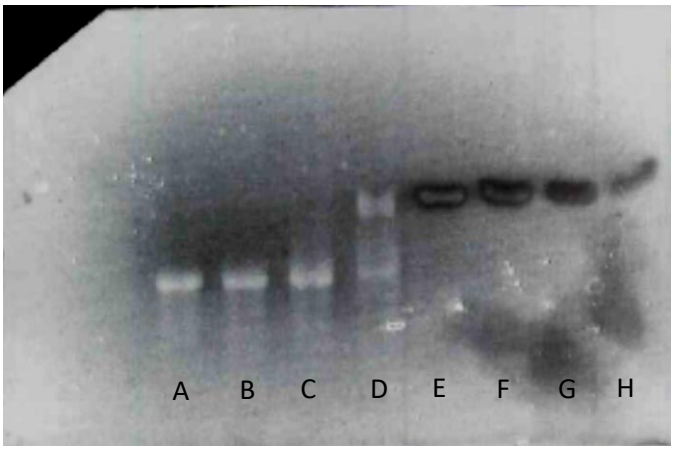

Figure 13: Oligonucleotide A_{50} and T_{50} (at 10 µM) incubated with TMPyP-Au at the concentrations below and run on a 20% polyacrylamide native gel.

From left **(A)** ssDNA A_{50} ,**(B)** ssDNA A_{50} with 50µM TMPyP-Au, **(C)** ssDNA A_{50} with 100µM TMPyP-Au, **(D)** ssDNA A_{50} with 200µM TMPyP-Au following **(E)** ssDNA T_{50} ,**(F)** ssDNA T_{50} with 50µM TMPyP-Au, **(G)** ssDNA T_{50} with 100µM TMPyP-Au, **(H)** ssDNA T_{50} with 200µM TMPyP-Au.

*The oligonucleotide A_{50} and T_{50} despite same size has different migration speed.

4.2 Incubation of oligonucleotide A_{50} with TMPyP-Au causes red shift at Q-band region:

Stepwise addition of oligonucleotide A_{50} to a constant concentration of TMPyP-Au resulted in a gradual shifting of the Soret and Q-band peaks towards higher wavelength regions of the spectrum. Only a very minor shift was observed in the same experiment when using T_{50} or a random oligonucleotide; no spectrum shift was observed in the negative control (milli-Q water only). The titration of 100µM TMPyP-Au with increasing concentration of oligonucleotide A_{50} from 0 to 3µM showed a shifting of the Q-band peak from 520 nm to 526 nm; in the case of oligonucleotide T_{50} the Q-band peak shifted only from 520 to 522nm (not shown).

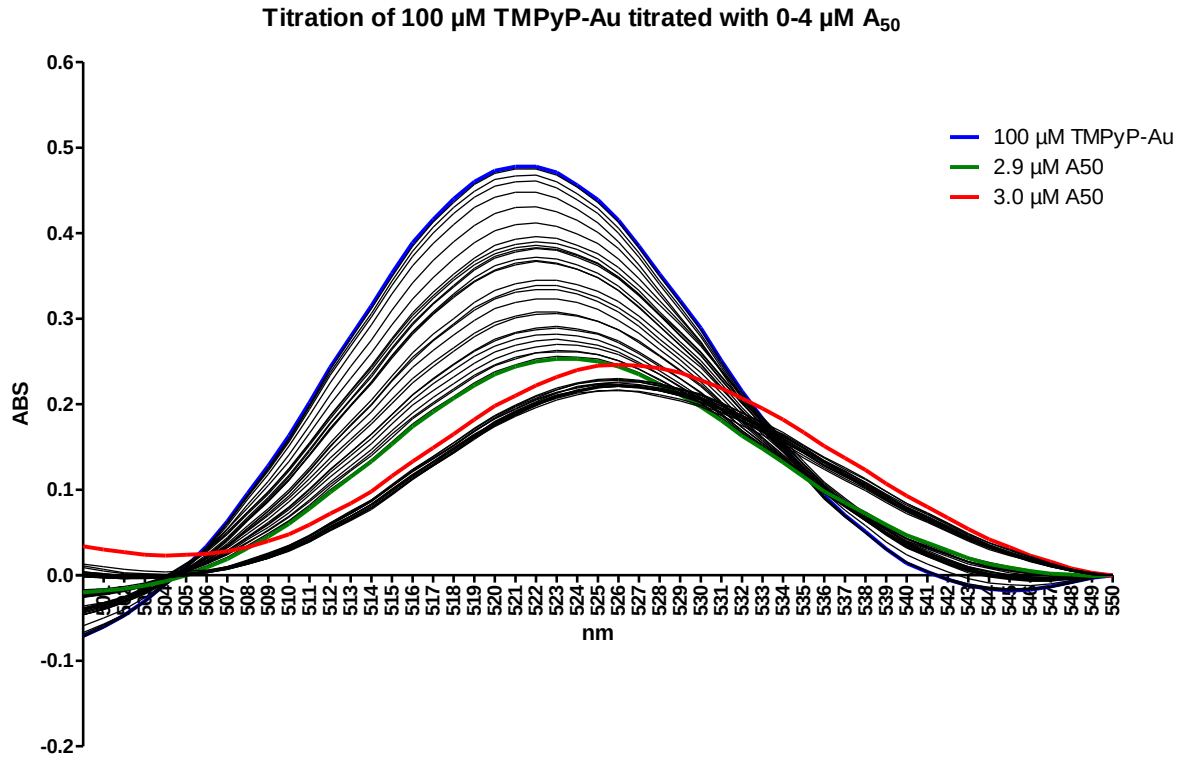

Figure 14.A: Spectrometric graph of TMPyP-Au Q-band titrated with ss DNA oligo A_{50}

The 100 µM TMPyP-Au (blue) was titrated with 1µM oligo A_{50} in 30 steps and the results were recorded. The absorption signal diminished due to binding of TMPyP-Au to the oligonucleotide. This causes the hypochromic and red shift effect. At 3 µM A_{50} became saturated with 100 µM TMPyP-Au, which is reflected in no further change in the above parameters.

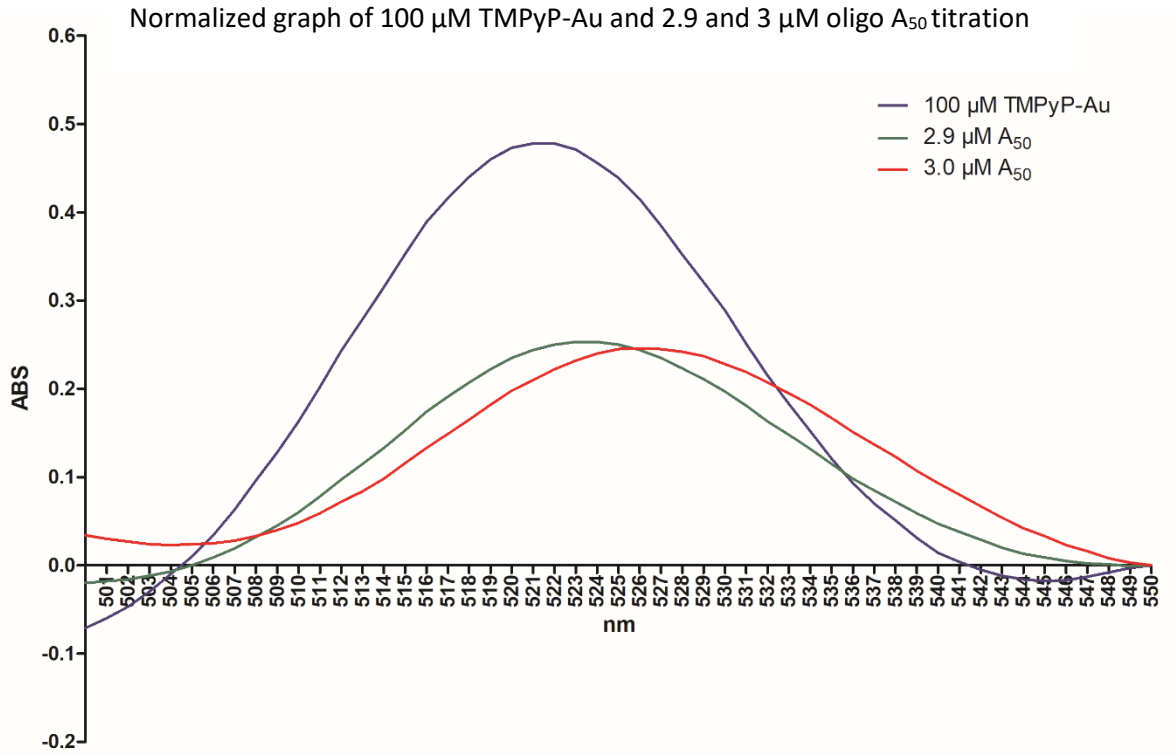

Figure 14B: Spectrometric graph of TMPyP-Au Q-band titrated with ss DNA oligo A_{50}

Only the 100 µM TMPyP-Au, 2.9 µM A_{50} (last step before saturation) and 3 µM A_{50} (saturation point) is plotted. Note that no further change occurred on addition of up to 4 µM A_{50} (see Fig. 14A).

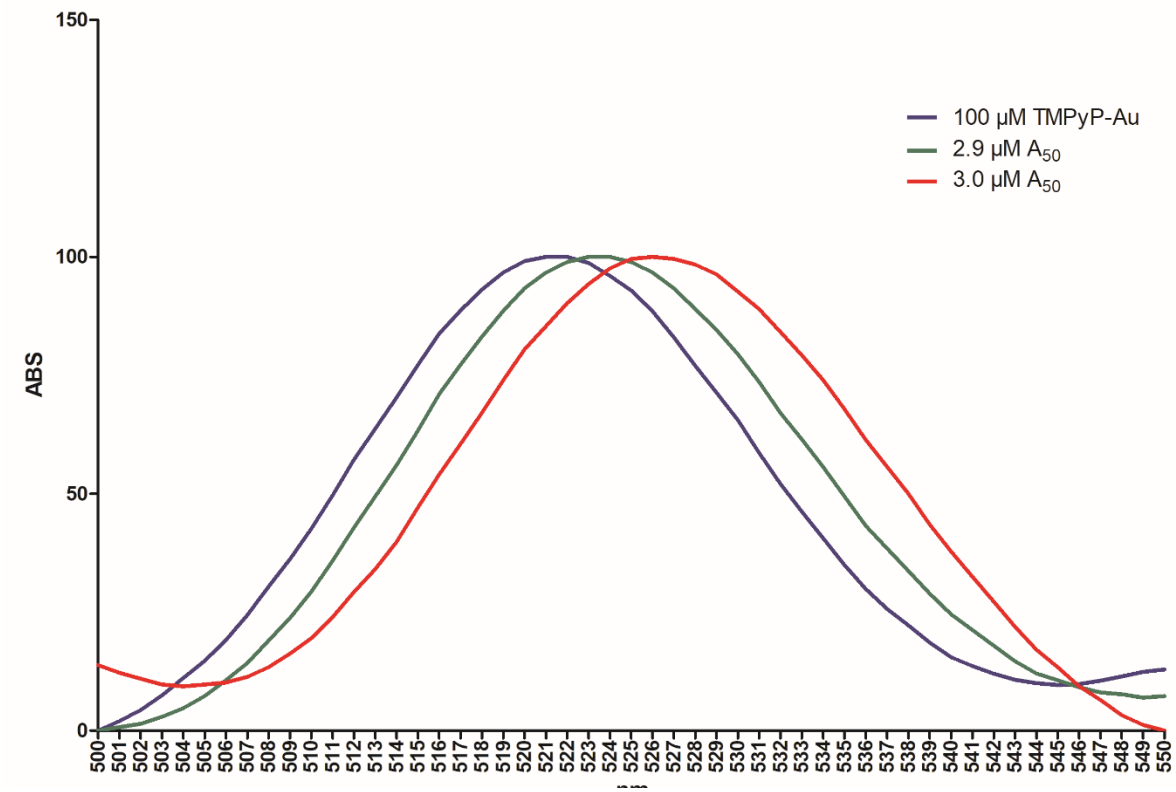

Figure 15: Data from Fig. 14B normalized as to take into account the dilution and hypochromicity (occurring because of stepwise addition of the A_{50} solution).

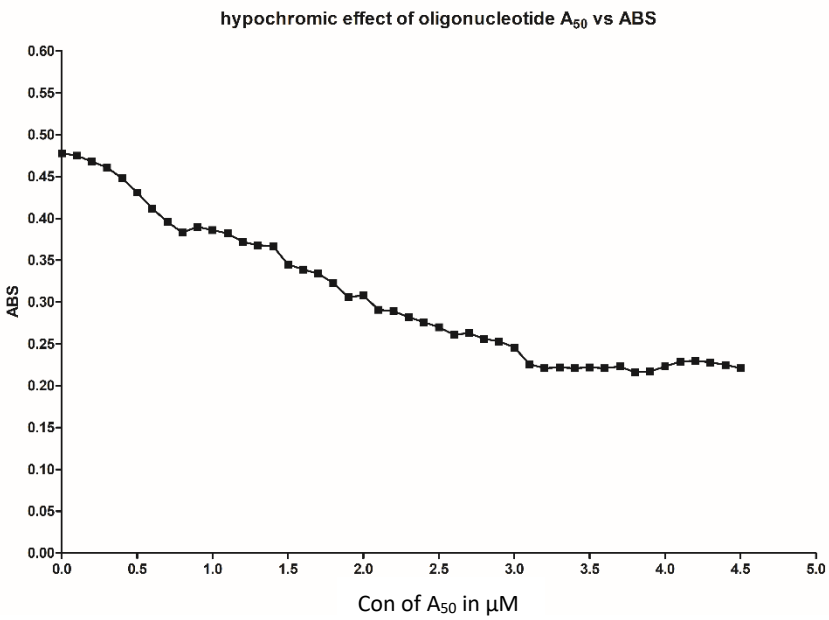

Figure 15B: Hypochromic effect of 100 µM TMPyP-Au titrated with ss DNA oligo A_{50}

Figure 15C: Red shift upon titration of 100 µM TMPyP-Au with ss DNA oligo A_{50}. Note the two plateaus where addition of A_{60} has no effect and the jump in the signal on exceeding a threshold

To confirm binding of TMPyP-Au to oligonucleotide A_{50}, we first titrated Au-porphyrin with A_{50} to saturation and recorded the peak shift. Then, we added, to the same solution, increasing amounts of the oligonucleotide T_{50}. The Q-band peak, which was shifted by titration using A_{50} from 520 to 526 nm was shifted back to the lower wavelength region of the spectrum from 526 to 521 nm (Fig 14C) This might be taken to indicate that T_{50} was hybridizing to the A_{50} and thereby replaced TMPyP-Au. It confirms the specific binding of TMPyP-Au to A_{50} and absence of binding to the A/T hybrid.

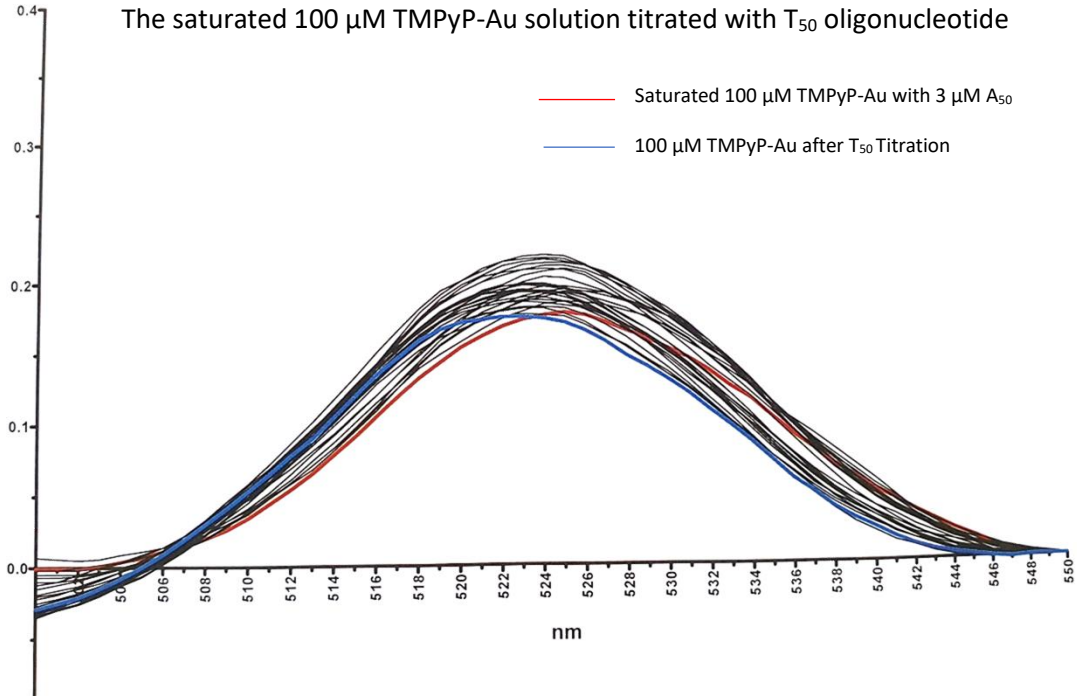

Figure 14C: Spectrometric graph of saturated TMPyP-Au Q-band titrated with ss DNA oligo T_{50}

The saturated 100 µM TMPyP-Au with 3 µM A_{50} (from pervious experiment 14B) titrated with 3 µM T_{50}. Note that the spectrum shifted back from 526 to 521.

4.3 Binding of either TMPyP-Cu or TMPyP-Au to A_{16} attenuates the H-signal in NMR spectroscopy:

The preferred oxidation state of the copper ion within the porphyrin-complex is 2+. Due to the presence of an unpaired electron in the d^9 orbital, the complex is strongly paramagnetic (Fig. 16, blue). This leads to relaxation of the NMR spectrum. Porphyrin-copper is weakly magnetized by an externally applied magnetic field, and forms internal, induced magnetism. Conversely, TMPyP-Au seems to prefer the 3+ oxidation state, which means d^8. It can be either dia- or paramagnetic (depending on the type of the ligands). It also depends on the energy difference between the dxy and the dx^2-y^2 orbital). It can have either the configuration: $dz2^2$ dxz^2 dyz^2 dxy^2 (diamagnetic) or $dz2^2$ dxz^2 dyz^2 dxy^1 $dx2\text{-}y2^1$ (paramagnetic). In the present case, it was diamagnetic (Fig. 16, red).

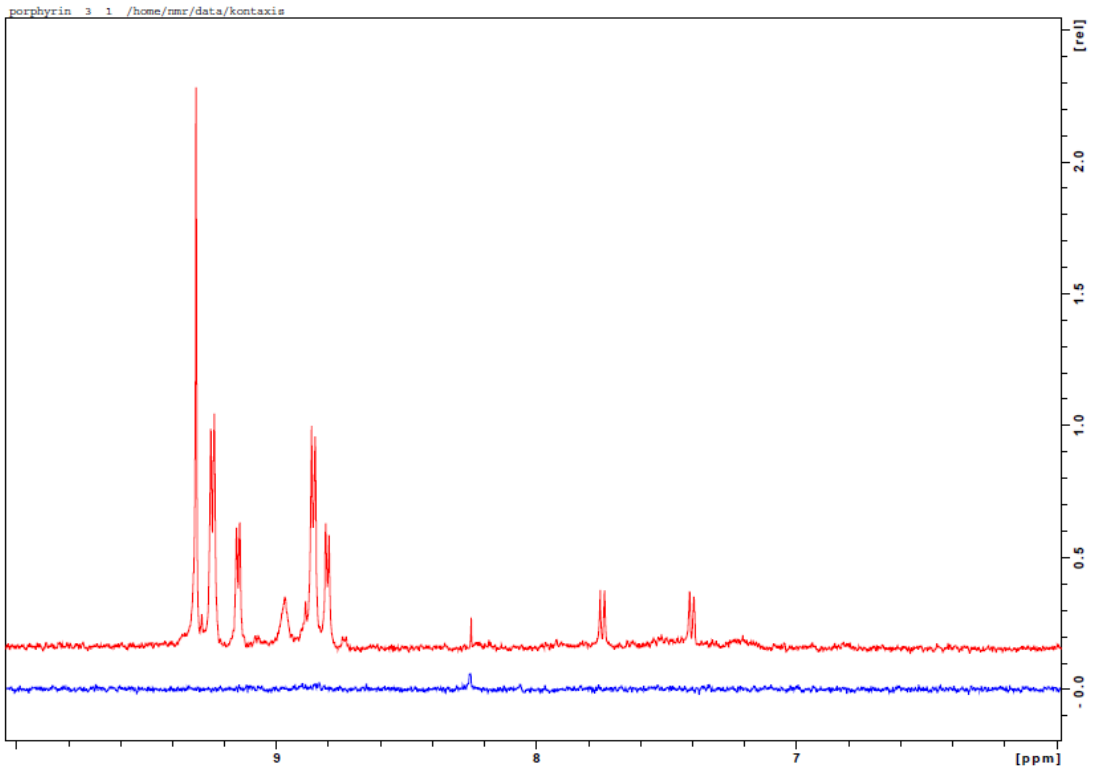

Figure 16: Paramagnetic Porphyrin-Cu signal (Blue) vs Diamagnetic TMPyP-Au signal (Red)

Under the chosen conditions the porphyrin-copper showed essentially no signal because of the high paramagnetic effect. On the other hand, TMPyP-Au is diamagnetic and exhibits a characteristic signal.

Being diamagnetic, the gold in TMPyP-Au is repelled by the magnetic field. This creates an induced magnetic field in the opposite direction. In the case of TMPyP-Cu, the strong paramagnetic effect of Cu^{2+} ions relaxes the signals stemming from oligonucleotides that get into close physical contact with it. Therefore, we titrated porphyrin-copper into the saturated solution of oligonucleotide. In case of binding, the oligonucleotide signal is lost, because binding of TMPyP-Cu relaxes the signals. As seen in Fig. 18A, most of the signals stemming from A_{16} are diminishing with increasing concentration of TMPyP-Cu. This is even better distinguishable when focussing on the peak at about 7.0 ppm (inset). In contrast, titration of TMPyP-Cu into the control random oligonucleotide only shows a very minor decrease of the signal (Fig. 18B). Note that the shape of the spectrum is different because of the different sequence/composition of the control oligonucleotide. Values shown in the inset are thus derived from the peak most affected by addition of TMPyP-Cu (at about 7.7 ppm). Our data thus confirm those by Zhu-Xin Zhou *el al.* (2) by using a different methodology.

As mentioned above, TMPyP-Au is diamagnetic. Therefore, we tested binding of TMPyP-Au via cross saturation of the gold. Although this method is not as sensitive, it is the only way of demonstrating binding by NMR. TMPyP-Au has distinct spectrum due to the diamagnetism. The oligonucleotides A_{16} and R_{16} were separately titrated with high concentrations of TMPyP-Au. The spectrum of the titration with A_{16} and R_{16}, respectively, makes it clear that A_{16} (red spectrum) is able to relax the TMPyP-Au spectrum by binding to the compound which R_{16} (blue spectrum) is not able to do this.

1) TMPyP-Au was incubated with A_{16} (red) and R_{16} (blue), respectively, and the LOGSY signal was recorded. Peaks between 8.5 and 9.5 ppm indicate that energy is being transfer from the nucleic acid to the porphyrin complex only from A_{16} but not from R_{16} implying specific binding of the porphyrin complex to the former.

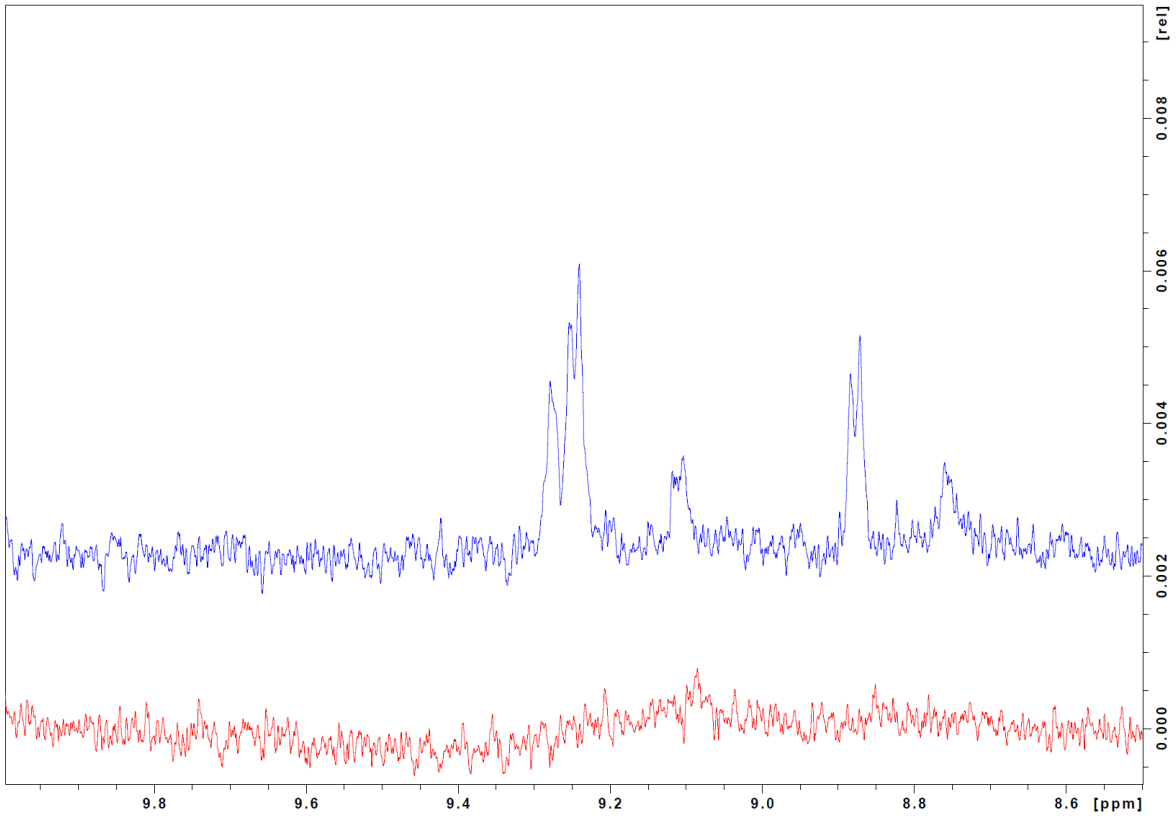

Figure 17: TMPyP-Au titrated with oligonucleotide R_{16} (blue) vs oligonucleotide A_{16} (red).

Adding oligonucleotide A_{16} caused depletion of TMPyP-Au signal were as the oligonucleotide R_{16} has no effect.

2) Paramagnetic relaxation enhancement. The above experiment cannot be performing with the Porphyrin-copper because of its paramagnetic feature, rather than diamagnetic properties. Increasing amounts of porphyrin-copper were added to a constant concentration of A_{16} (A) and R_{16} (B) oligonucleotides and the relaxation signal was recorded. Whereas the signal was quenched substantially in a concentration-dependent manner on addition of porphyrin-copper to A_{16} no such quenching was seen with R_{16}. However, the much lower signal intensity and broader peaks of the R_{16} sample might also indicate aggregation and/or the formation of base paired regions.

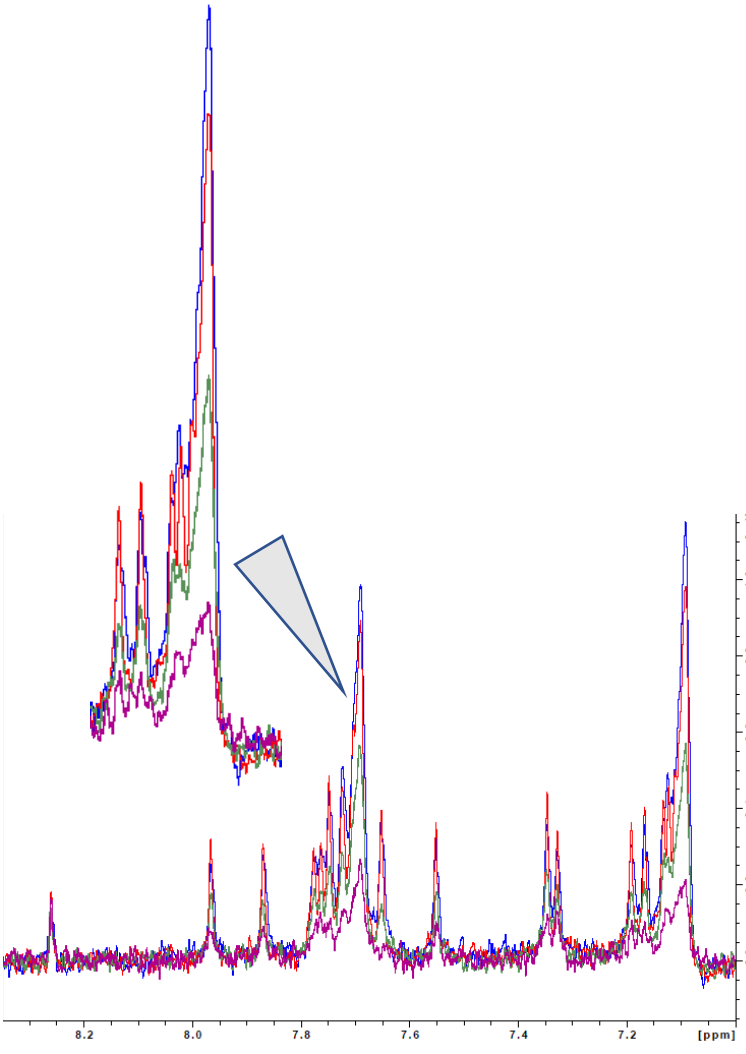

Figure 18A: Titration of ss DNA A_{16} with TMPyP-Cu

The TMPyP-Cu was titrated in 16 steps in ss DNA oligo A_{16} which results in depletion of oligo A_{16} signal

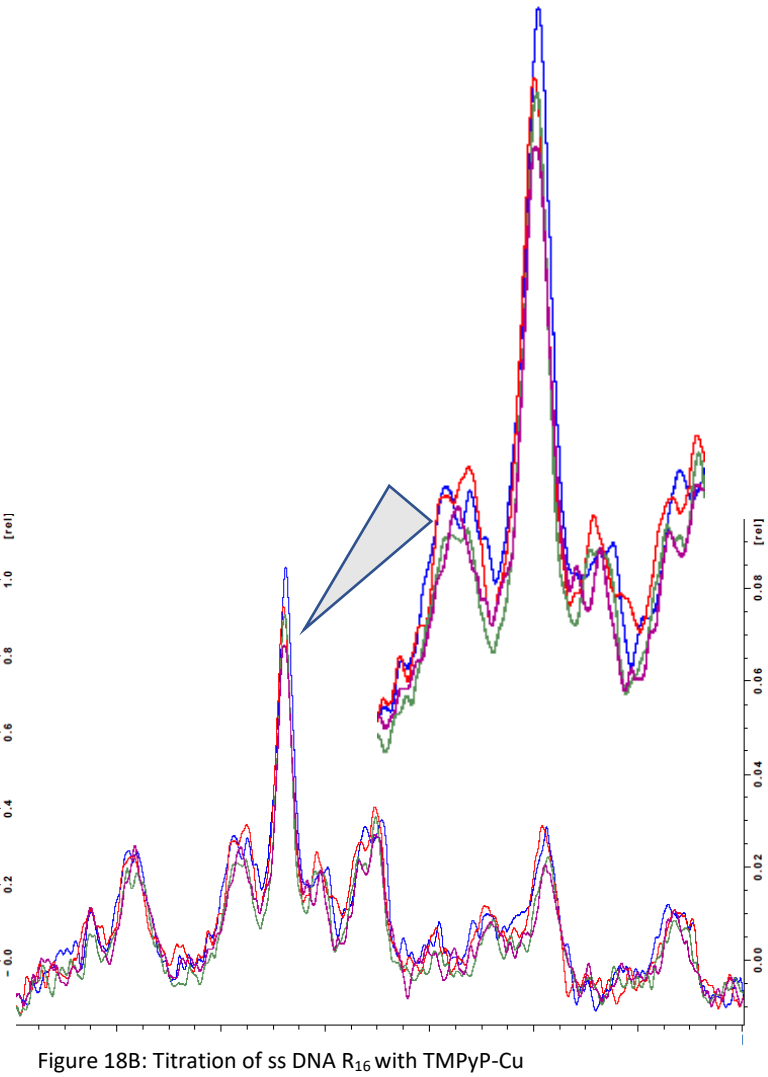

Figure 18B: Titration of ss DNA R_{16} with TMPyP-Cu

The TMPyP-Cu titrated in 16 steps in ss DNA oligo R_{16} only marginal depletion of oligo R_{16} signal.

* For sake of clarity, only step 1, 6, 11, and 16 are shown.

4.4 Poly-(A) adopts secondary structures on incubation with TMPyP-Au:

Attempting at detecting binding of nano-gold to poly-(A) RNA Sofiya Fedosyuk, (D. Blaas group) used incorporation of 2-Ethynyl-ATP (2-EATP) by *in vitro* synthesis of the poly-(A) followed by treatment with azide-biotin and incubation with streptavidin-gold conjugates. Rotary shadowing EM was done by using platinum. As shown in the two panels of Fig. 20, corresponding to two experiments, there are indeed some instances where gold particles appear to bind to the poly-(A) RNA. Whether this binding takes place at particularly high concentrations of biotin occurring by the statistical distribution of incorporation of the 2-EATP is currently unclear.

In order to label adenines without any modification, we treated plain poly-(A) with TMPyP-Au. To avoid coiling up of the RNA, which can occur with very long molecules, the RNA was fragmented to roughly 200 nt prior to the experiment. We assumed that binding of the gold complexes to the RNA might be visible due to the high density of the gold. Unfortunately, I did not see any change in thickness of the poly-(A) when incubated with TMPyP-Au (compare panels A, B in Fig. 22, with panels A, B in Fig. 23). However, there was a clear induction of secondary structure in the presence of TMPyP-Au. Whereas plain poly-(A) showed up as linear strands, addition of TMPyP-Au appeared to result in folding back of the RNA on itself as also suggested by the small loops at some of the ends (red arrows). This is also supported by these strands appearing to be thicker than the others (compare strands ending with a loop with possibly single strands indicated with yellow arrows). Alternatively, the thicker filaments could also be the result of the pairing of different strands. *In-vitro* synthesized ss RNA used as negative control in this experiment.

The electron microscopy done using a rotary shadowing method to enhance the resolution of ssRNA under the microscope to coat the grids and RNA using platinum or tungsten. Using tungsten as a coating layer was not successful as the tungsten granules size were covering both grid and RNA strands and possible effect of TMPyP-Au was covered with tungsten coating. After doing several platinum coatings, the optimal coating thickness found out with 0.7 mm. The observation of many grids led us to different conclusion comparing the former approaches. At first, due to different sample treatments before the observation, we were not observing the RNA samples on some grids, which may due to RNase contamination

during treatment steps. We also using spectrometry showed that presence of salts like PBS or potassium phosphate buffer interfering and probably inhibiting binding of TMPyP-Au to the ssDNA, therefore, no spectrum shift observed but using a buffer to spray samples on mica sheet was a mandatory part in grid preparation.

The treating of poly-(A) ssRNA with TMPyP-Au, causes the formation of secondary structure within the RNA strands. This may confirm the EMSA results, where the presence of more TMPyP-Au shifting the ssDNA adenine strands by making more secondary structures therefore bands migrate slower through the gel pores.

The TMPyP-Au may act as intercalator, which means it attaching ssDNA or RNA strands due to its affinity but not wrapping a single strand of DNA or RNA. This interpretation was based on the EMSA and EM results. A poly-(A) bulk structure shape is visible in some figures.

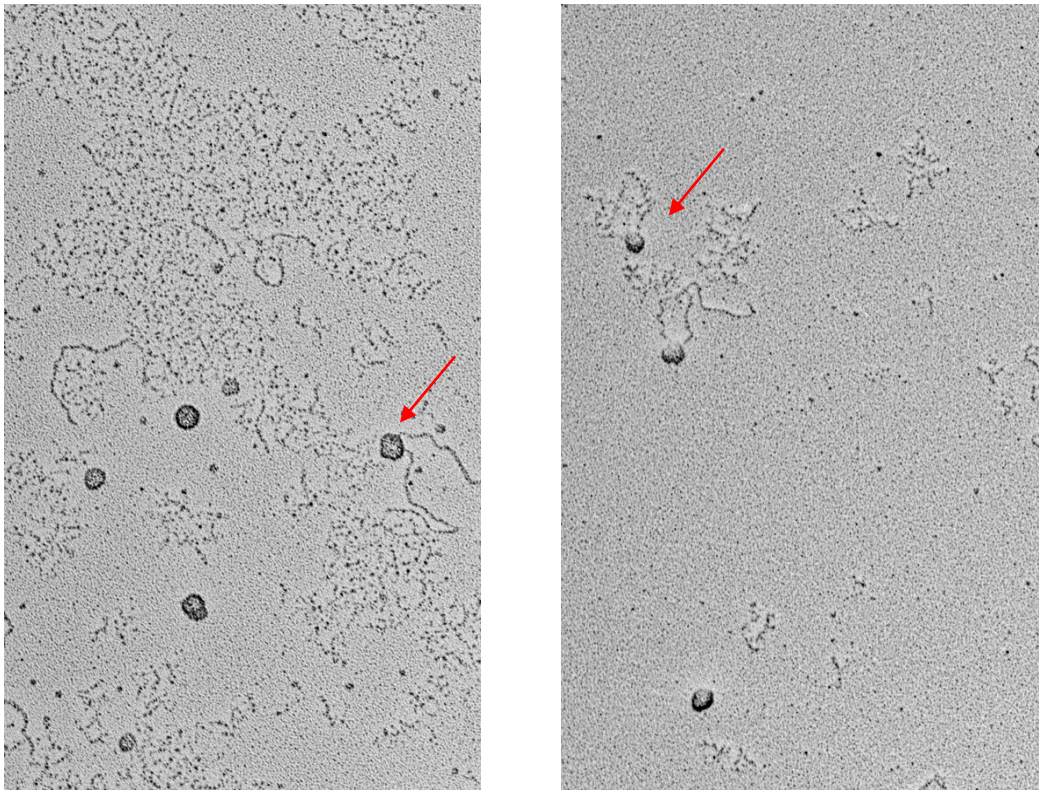

Figure 20: Poly-(A) RNA was synthesized in the presence of 2-EATP to allow for subsequent incorporation of biotin. This RNA was then treated with streptavidin-gold conjugates (Sofiya Fedosyuk, D. Blaas group), Morgagni 268D, 71kX. In some instances, the nano-gold appears to bind to the poly-(A) presumably where statistically more 2-Ethynyl-ATP had been incorporated. Micrographs from two different experiments are shown.

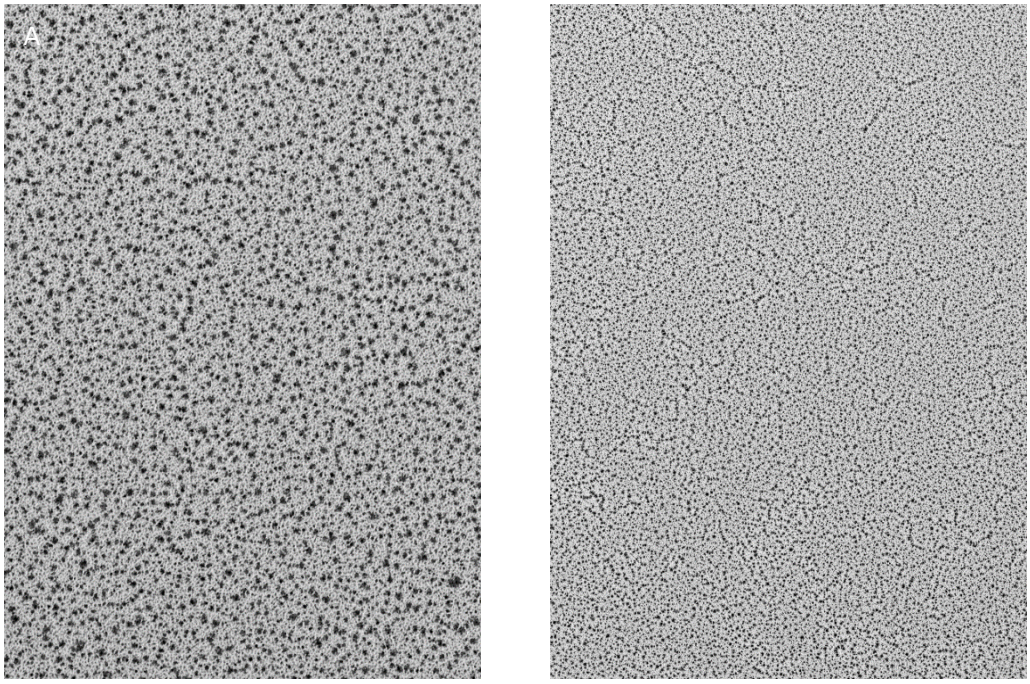

Figure 21: The poly-(A) RNA treated with 200 µM TMPyP-Au and rotary shadowed with tungsten at 1.2 nm thickness, Morgagni 268D, 71kx (A) and 28Kx (B). The tungsten coating appeared not useful for observation of RNA due to large granule size of tungsten.

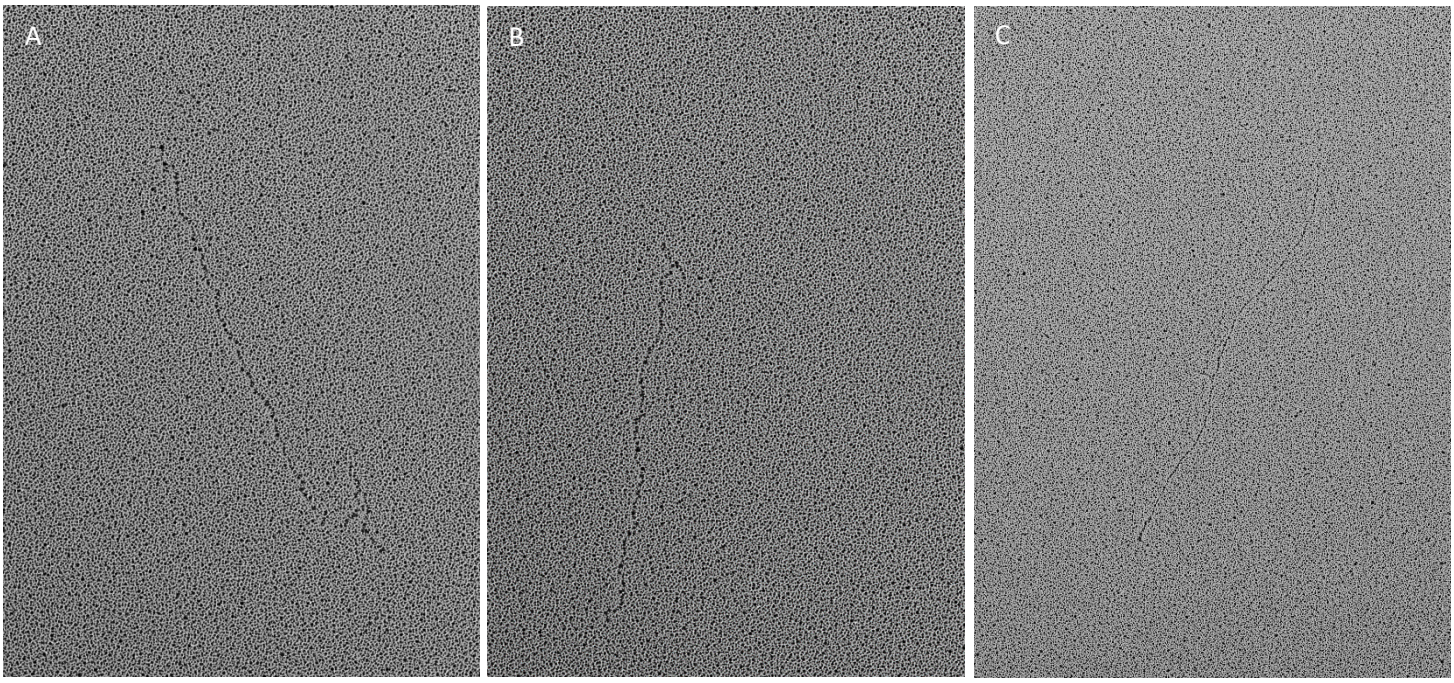

Figure 22: The poly-(A) RNA, (A and B) and *in vitro* synthesized random sequence RNA (C), rotary shadowed with platinum at 0.7 nm, Morgagni 268D, 71kX, Scale bar 500 nm

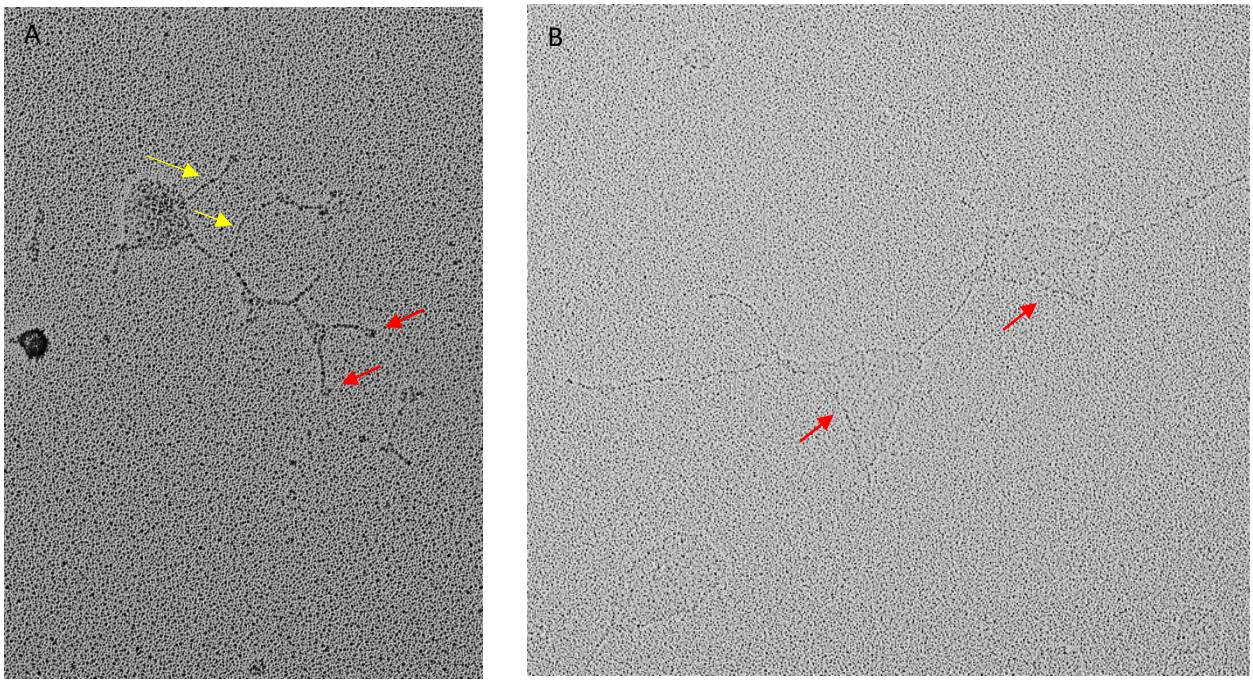

Figure 23: poly-(A) RNA incubated with 200 µM TMPyP-Au, rotary shadowed with 0.7 nm platinum, Morgagni 268D, 71kX. Poly-(A) RNA was incubated with TMPyP-Au, sprayed, dried, and coated with 0.7 nm platinum. The TMPyP-Au treatment causes formation of secondary structures within the poly-(A). Micrographs from two experiments are shown. Red arrows, loops (?); yellow arrows, single strands (?). Scale bar 500 nm

5. Discussions and further ideas:

In this study, by using EMSA, light and NMR spectrometry, we have shown that TMPyP-Au has much higher affinity for poly-(A) when compared to other oligonucleotide sequences. By using rotary shadowing electron microscopy, we found that TMPyP-Au leads to structuring of poly-(A) presumably by inducing self-structures, as seen from increased thickness. However, we were not able to observe an anticipated increase in thickness/density as a consequence of binding of TMPyP-Au to single poly-(A) strands. One of the most interesting observations was it that increasing the ratio of TMPyP-Au to poly-(dA) led to non-linear decrease in migration on non-denaturing gels and an increase in red shift in the spectra. Two clearly distinguishable plateaus were observed that might be indicating that distinct secondary structures are adopted. Apparently, a gross conformational change occurs at a threshold in the stoichiometry. The original goal, namely the labelling of the poly-(A) within native rhinovirus and/or A-particles was not met due to

Whether the higher affinity of TMPyP-Au for oligo-(dA) and oligo-(rA), as compared to other oligo-nucleotides is simply due to preferred binding to adenosine or to the property of poly-(A) adopting self-structures is unclear.

The NMR experiments confirm the previous finding (7) of specific binding of the copper complex as well as my above demonstration of similar specificity of gold porphyrins. It is possible that this is merely due to the lack of secondary structure of poly-(A) as compared to the randomized oligonucleotide. The latter will have several possibilities of intra- and inter-molecular base pairing. This would result in reduced accessibility of the nitrogen ring and thus reduced signal quenching. To find out whether this is indeed the case, one needs testing A_{16}/T_{16} hybrids (these should give the same result as R_{16}) and T_{16} in which nucleotides should be similarly accessible as in A_{16}.

By analysing the EMSA and spectrometric results, we observed two saturation points at which TMPyP-Au binding caused dA_{50} molecules to bind to each other and caused band shifts in EMSA or a red shift in spectrometry. The stoichiometry at the saturation point was estimated, based on EMSA and spectrometry results, to be about 20:1 (TMPyP-Au 200 µM: 10 µM A_{50}) and concentration wise 33 : 1 (TMPyP-Au 100 µM : 3 µM A_{50}), respectively. The latter

could not be verified by gel-shift experiments due to precipitation of the reactants. The calculation number of each TMPyP-Au and A_{50} molecules shows a possible 1:1 binding ratio.

Affinity measurements of poly-(A) RNA for TMPyP-Au are tedious because of the low stability of RNA and the risk of contamination with RNases. We have thus considered other approaches, among these atomic force microscopy (AFM) and plasma resonance spectroscopy (PRS). The first has been initiated via cooperating with Peter Hinterdorfer's group in Linz. The method allows for thickness measurements and will show whether treated and untreated RNA strands have indeed different dimensions. On the other hand, PRS might give more quantitative results with respect to the ligand and receptor binding ratio.

Within the time frame of this thesis, we carried out only one single cryo-electron microscopy experiment to eventually see asymmetric localization of density stemming from TMPyP-Au attachment to the poly-(A) tail of the viral RNA. However, except from some unspecific binding of the complex to the surface of A-particles we were unable to detect any asymmetric distribution. More experiments will thus be necessary to find out whether TMPyP-Au would indeed density-label the poly-(A) tail of the viral genomic RNA under various conditions, including incubation of 3'-RNA fragments of suitable length.

6. Supporting information:

Meso-5,10,15,20-tetrakis(4-N-methyl-pyridiniumyl) porphyrinatogold (III) pentachloride synthesis:

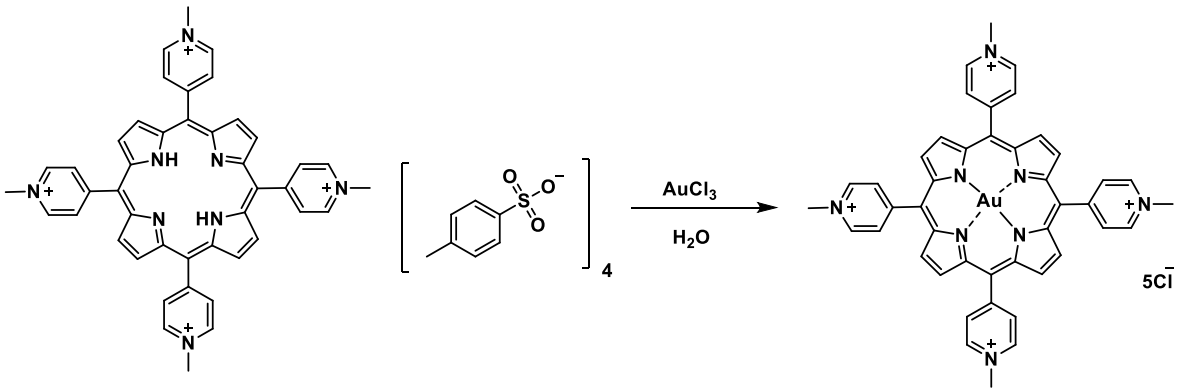

TMPyP - meso-Tetra(N-methyl-4-pyridyl) porphine tetratosylate - (47 mg, 0.035 mmol) and AuCl3 (23 mg, 0.077 mmol, 2.2 equiv.) were dissolved in distilled water (7 ml) under argon atmosphere and the reaction mixture was let refluxed for 24 hours in the dark. The reaction was monitored by UV-VIS and was complete when the Soret band shifted from 424 nm to 404 nm. After cooling down, 2M aq. solution of $NaClO_4$ (15 ml) was added whereas a red precipitate formed. The precipitate was then washed with 2% aq. solution of $NaClO_4$ (3x10 mL) and perchlorate anions where then exchanged for chloride anions upon treatment with ion exchange resin (IRA 400 Cl- form, 2x5 g; the resin was twice washed with 0.5 N HCl and then with dist. water to neutral pH). Water was then evaporated, yielding 37 mg of red solid.
Technical University of Vienna (Cintulová, Daniela)

Yield 37 mg (95%) red solid

Sum formula, m.w. C44H36AuN8Cl5, 1048.79 g/mol

UV VIS 404 nm max.

^{1}H-NMR (CD3OD, 400 MHz): δ 9.68 (s, 8H), 9.52 (d, J = 6.5 Hz, 8H), 9.10 (d, J = 6.7 Hz, 8H), 4.87 (s, 12H).

Acknowledgment:

I wanted to thank Marlene Brandstetter from Electron Microscopy Facility (VBCF) for her help during EM observations. I would also like to thank Daniela Cintulová from Technical University of Vienna for synthesising of TMPyP-Au complex.

References:

1. Hainfeld, J. F. (1996). Labeling with nanogold and undecagold: techniques and results. *Scanning Microsc Suppl, 10*, 309-322; discussion 322-305. Retrieved from https://www.ncbi.nlm.nih.gov/pubmed/9601549.
2. Mercogliano, C. P., & DeRosier, D. J. (2007). Concatenated metallothionein as a clonable gold label for electron microscopy. *J Struct Biol, 160*(1), 70-82. Retrieved from https://www.ncbi.nlm.nih.gov/pubmed/17692533. doi:10.1016/j.jsb.2007.06.010
3. Grabenbauer, M. (2012). Correlative light and electron microscopy of GFP. *Methods Cell Biol, 111*, 117-138. Retrieved from https://www.ncbi.nlm.nih.gov/pubmed/22857926. doi:10.1016/B978-0-12-416026-2.00007-8
4. Meisslitzer-Ruppitsch, C., Rohrl, C., Neumuller, J., Pavelka, M., & Ellinger, A. (2009). Photooxidation technology for correlated light and electron microscopy. *J Microsc, 235*(3), 322-335. Retrieved from https://www.ncbi.nlm.nih.gov/pubmed/19754726. doi:10.1111/j.1365-2818.2009.03220.x
5. Adams, S. R., Mackey, M. R., Ramachandra, R., Palida Lemieux, S. F., Steinbach, P., Bushong, E. A., . . . Tsien, R. Y. (2016). Multicolor Electron Microscopy for Simultaneous Visualization of Multiple Molecular Species. *Cell Chem Biol, 23*(11), 1417-1427. Retrieved from https://www.ncbi.nlm.nih.gov/pubmed/27818300. doi:10.1016/j.chembiol.2016.10.006
6. Ngo, J. T., Adams, S. R., Deerinck, T. J., Boassa, D., Rodriguez-Rivera, F., Palida, S. F., . . . Tsien, R. Y. (2016). Click-EM for imaging metabolically tagged nonprotein biomolecules. *Nat Chem Biol, 12*(6), 459-465. Retrieved from https://www.ncbi.nlm.nih.gov/pubmed/27110681. doi:10.1038/nchembio.2076
7. Zhou, Z. X., Gao, F., Chen, X., Tian, X. J., & Ji, L. N. (2014). Selective binding and reverse transcription inhibition of single-strand poly(A) RNA by metal TMPyP complexes. *Inorg Chem, 53*(19), 10015-10017. Retrieved from https://www.ncbi.nlm.nih.gov/pubmed/25203754. doi:10.1021/ic501337c
8. Rybicki, E. (2015). *A Short History of the Discovery of Viruses*(Vol. 1, pp. 43).
9. Nichol, K. L., D'Heilly, S., & Ehlinger, E. (2005). Colds and influenza-like illnesses in university students: impact on health, academic and work performance, and health care use. *Clin Infect Dis, 40*(9), 1263-1270. Retrieved from https://www.ncbi.nlm.nih.gov/pubmed/15825028. doi:10.1086/429237
10. Roelen, C. A., Koopmans, P. C., Notenbomer, A., & Groothoff, J. W. (2011). Job satisfaction and short sickness absence due to the common cold. *Work, 39*(3), 305-313. Retrieved from https://www.ncbi.nlm.nih.gov/pubmed/21709366. doi:10.3233/WOR-2011-1178
11. Fendrick, A. M., Monto, A. S., Nightengale, B., & Sarnes, M. (2003). The economic burden of non-influenza-related viral respiratory tract infection in the United States. *Arch Intern Med, 163*(4), 487-494. Retrieved from https://www.ncbi.nlm.nih.gov/pubmed/12588210.
12. Pappas, D. E., Hendley, J. O., Hayden, F. G., & Winther, B. (2008). Symptom profile of common colds in school-aged children. *Pediatr Infect Dis J, 27*(1), 8-11. Retrieved from https://www.ncbi.nlm.nih.gov/pubmed/18162930. doi:10.1097/INF.0b013e31814847d9
13. Palmenberg, A. C., Spiro, D., Kuzmickas, R., Wang, S., Djikeng, A., Rathe, J. A., . . . Liggett, S. B. (2009). Sequencing and analyses of all known human rhinovirus genomes reveal structure and evolution. *Science, 324*(5923), 55-59. Retrieved from https://www.ncbi.nlm.nih.gov/pubmed/19213880. doi:10.1126/science.1165557

14. Simmonds, P., McIntyre, C., Savolainen-Kopra, C., Tapparel, C., Mackay, I. M., & Hovi, T. (2010). Proposals for the classification of human rhinovirus species C into genotypically assigned types. *J Gen Virol, 91*(Pt 10), 2409-2419. Retrieved from https://www.ncbi.nlm.nih.gov/pubmed/20610666. doi:10.1099/vir.0.023994-0

15. Bochkov, Y. A., & Gern, J. E. (2012). Clinical and molecular features of human rhinovirus C. *Microbes Infect, 14*(6), 485-494. Retrieved from https://www.ncbi.nlm.nih.gov/pubmed/22285901. doi:10.1016/j.micinf.2011.12.011

16. Wang, L., & Smith, D. L. (2005). Capsid structure and dynamics of a human rhinovirus probed by hydrogen exchange mass spectrometry. *Protein Sci, 14*(6), 1661-1672. Retrieved from https://www.ncbi.nlm.nih.gov/pubmed/15883190. doi:10.1110/ps.051390405

17. Pickl-Herk, A., Luque, D., Vives-Adrian, L., Querol-Audi, J., Garriga, D., Trus, B. L., . . . Caston, J. R. (2013). Uncoating of common cold virus is preceded by RNA switching as determined by X-ray and cryo-EM analyses of the subviral A-particle. *Proc Natl Acad Sci U S A, 110*(50), 20063-20068. Retrieved from https://www.ncbi.nlm.nih.gov/pubmed/24277846. doi:10.1073/pnas.1312128110

18. Harutyunyan, S., Kowalski, H., & Blaas, D. (2014). The Rhinovirus subviral a-particle exposes 3'-terminal sequences of its genomic RNA. *J Virol, 88*(11), 6307-6317. Retrieved from https://www.ncbi.nlm.nih.gov/pubmed/24672023. doi:10.1128/JVI.00539-14

19. Hofer, F., Gruenberger, M., Kowalski, H., Machat, H., Huettinger, M., Kuechler, E., & Blaas, D. (1994). Members of the low density lipoprotein receptor family mediate cell entry of a minor-group common cold virus. *Proc Natl Acad Sci U S A, 91*(5), 1839-1842. Retrieved from https://www.ncbi.nlm.nih.gov/pubmed/8127891.

20. Bochkov, Y. A., Watters, K., Ashraf, S., Griggs, T. F., Devries, M. K., Jackson, D. J., . . . Gern, J. E. (2015). Cadherin-related family member 3, a childhood asthma susceptibility gene product, mediates rhinovirus C binding and replication. *Proc Natl Acad Sci U S A, 112*(17), 5485-5490. Retrieved from https://www.ncbi.nlm.nih.gov/pubmed/25848009. doi:10.1073/pnas.1421178112

21. Fuchs, R., & Blaas, D. (2010). Uncoating of human rhinoviruses. *Rev Med Virol, 20*(5), 281-297. Retrieved from https://www.ncbi.nlm.nih.gov/pubmed/20629045. doi:10.1002/rmv.654

22. Jacobs, S. E., Lamson, D. M., St George, K., & Walsh, T. J. (2013). Human rhinoviruses. *Clin Microbiol Rev, 26*(1), 135-162. Retrieved from https://www.ncbi.nlm.nih.gov/pubmed/23297263. doi:10.1128/CMR.00077-12

23. Inal, J. M., & Jorfi, S. (2013). Coxsackievirus B transmission and possible new roles for extracellular vesicles. *Biochem Soc Trans, 41*(1), 299-302. Retrieved from https://www.ncbi.nlm.nih.gov/pubmed/23356301. doi:10.1042/BST20120272

24. Blaas, D., & Fuchs, R. (2016). Mechanism of human rhinovirus infections. *Mol Cell Pediatr, 3*(1), 21. Retrieved from https://www.ncbi.nlm.nih.gov/pubmed/27251607. doi:10.1186/s40348-016-0049-3

25. Smith, K. M. (1975). *Porphyrins and Metalloporphyrins*: Elsevier Scientific.

26. Goldoni, A. Porphyrins: fascinating molecules with biological significance. Retrieved from http://missionignition.net/she/articles/iron_porphyrin.pdf.

27. J.P. Collman et al., Metal Ions in Biology, Vol. 2, T.G. Spiro Ed., Wiley, NY, 1 (1980), M.A. Schiavon et al., J. Molecular Catalysis A, 174, 213, (2001), T.H. Richardson et al., Thin Solid Films, 393, 259, (2001)

28. K.S. Suslick, et al., "Shape Selective Oxidation Catalysis" in Comprehensive Supramolecular Chemistry, Vol. 5, K.S. Suslick Ed., Elsevier, Oxford, 141 (1996), P. Bhyrappa et al., J. Am. Chem. Soc., 118, 5708, (1996), J.A.A. Elemans et al., Org. Chem. 64, 7009, (1999)

29. Nonlinear Optical Materials and Devices for Applications in Information Technology. (1995). (K. R. W. A. Miller, B. Daino Ed. Vol. 289): Springer Netherlands.

30. D. Gust et al., Topics in Current Chemistry, 159, 103, (1991), M.R. Wasielewski, Chem. Rev., 92, 435, (1992), W. Han et al., J. Phys. Chem. B, 101, 10719, (1997), G. Stainberg-Yfrach et al., Nature, 392, 479, (1998)

31. Abelson, J. (2014). Methods in Enzymology. In (Vol. 541, pp. 179-196).

32. Tang, W., Zhou, H., & Li, W. (2015). Silver and Cyanine Staining of Oligonucleotides in Polyacrylamide Gel. *PLoS One, 10*(12), e0144422. Retrieved from https://www.ncbi.nlm.nih.gov/pubmed/26650843. doi:10.1371/journal.pone.0144422

33. RNA Methodologies, Robert E. Farrell, Jr

34. Caetano-Anollés (1994)Caetano-Anollés, G. a. M. G., P. (1994). Staining Nucleic Acids with Silver: An Alternative to Radioisotopic and Fluorescent Labeling Promega Notes Magazine, 13. Retrieved from https://pdfs.semanticscholar.org/6000/997d6a355bb529c12f8f25ea0b486f93c0c0.pdf.

35. Huang, R., Bonnichon, A., Claridge, T. D., & Leung, I. K. (2017). Protein-ligand binding affinity determination by the waterLOGSY method: An optimised approach considering ligand rebinding. Sci Rep, 7, 43727. Retrieved from https://www.ncbi.nlm.nih.gov/pubmed/28256624. doi:10.1038/srep43727